ISPRS Journal of Photogrammetry and Remote Sensing 196 (2023) 306–324

Contents lists available at ScienceDirect

ISPRS Journal of Photogrammetry and Remote Sensing

journal homepage: www.elsevier.com/locate/isprsjprs

Comparison of detectability of ship wake components between C-Band and X-Band synthetic aperture radar sensors operating under different slant ranges

Björn Tings *, Andrey Pleskachevsky, Stefan Wiehle

German Aerospace Center (DLR), Am Fallturm, 9, 28329 Bremen, Germany

ARTICLE INFO

Keywords:
Detectability modelling
Machine learning
Maritime object detection
Ship wake detection
Synthetic aperture radar

ABSTRACT

The detectability of wake components is affected by influencing parameters, which can be categorized into ship properties, environmental conditions and image acquisition settings. The characteristics of influences of most influencing parameters on the detectability are established. However, a consequent investigation and systematization of influences regarding differences in settings of various SARs have not been published.

In this study, data from four different SARs missions, namely TerraSAR–X (TSX), CosmoSkymed (CSK), Sentinel–1 (S1) and RADARSAT–2 (RS2), were collected and analyzed with focus on detectability of ship wake components. The sensors operate on different orbit altitudes and radar frequency bands: TSX and CSK work with X–Band, S1 and RS2 work with C–Band. Using methods from the field of Data Science, the detectability of wake components is modelled for each of the four sensors using machine leaning by the support vector machine (SVM) method. The created SVM-models are then compared in order to derive statements regarding relative detectability of individual wake components. A measure of detectability model's uncertainty and an alternative analysis based on accumulated backscattering statistics is presented to support the derived statements.

In conclusion, sensors with shorter slant ranges and X–Band in comparison to C–Band were found to be better suited for the detection of ship wakes. However, these characteristics only hold for wake components detectable due to the Bragg scattering mechanism, i.e. Kelvin wake arms and V-narrow wakes. No significant difference for near and far field of turbulent wakes is recognized.

1. Introduction

Spaceborne synthetic aperture radar (SAR) is a powerful instrument for monitoring seas. The newest methods for processing SAR data with increased precision allow detecting maritime objects and estimating environmental meteo-marine information with local variabilities in near real time (Pleskachevsky, et al., 2022). For large areas, in oceans where no in-situ measurements are available, this information source is indispensable for global shipping and other maritime activity.

The study at hand combines methods for estimation of meteo-marine parameters with the task of indirect detection of moving ships by their wake signatures. Objective of this study is comparison of detectability of ship wake components between different SAR sensors, which are operating on different orbit altitudes and with either X–Band or C–Band SAR onboard.

As in the article a variety of abbreviations and notations are used, Table A1 is attached in the appendix for nomenclature.

1.1. On detectability of ship wakes in SAR

The detectability of ships and their wakes in SAR imagery is influenced by several parameters, which can be categorized into ship properties, environmental conditions and SAR acquisition settings. (Tings, et al., 2018; Tings, et al., 2019; Tings, 2021). Ship wakes are the result of multiple interacting wave systems closely beneath and on the ocean surface, produced by the interaction of the ship's hull with the water. In studies on ship wakes in SAR imagery four wake components are distinguished: turbulent wake, Kelvin wake, V-narrow wake and internal waves wake (Lyden, et al., 1988). Fig. 1 shows a schematic representation of the various wake components recognized in SAR imagery.

* Corresponding author.
E-mail addresses: bjoern.tings@dlr.de (B. Tings), andrey.pleskachevsky@dlr.de (A. Pleskachevsky), stefan.wiehle@dlr.de (S. Wiehle).

https://doi.org/10.1016/j.isprsjprs.2022.12.008
Received 22 July 2022; Received in revised form 7 November 2022; Accepted 12 December 2022
Available online 13 January 2023

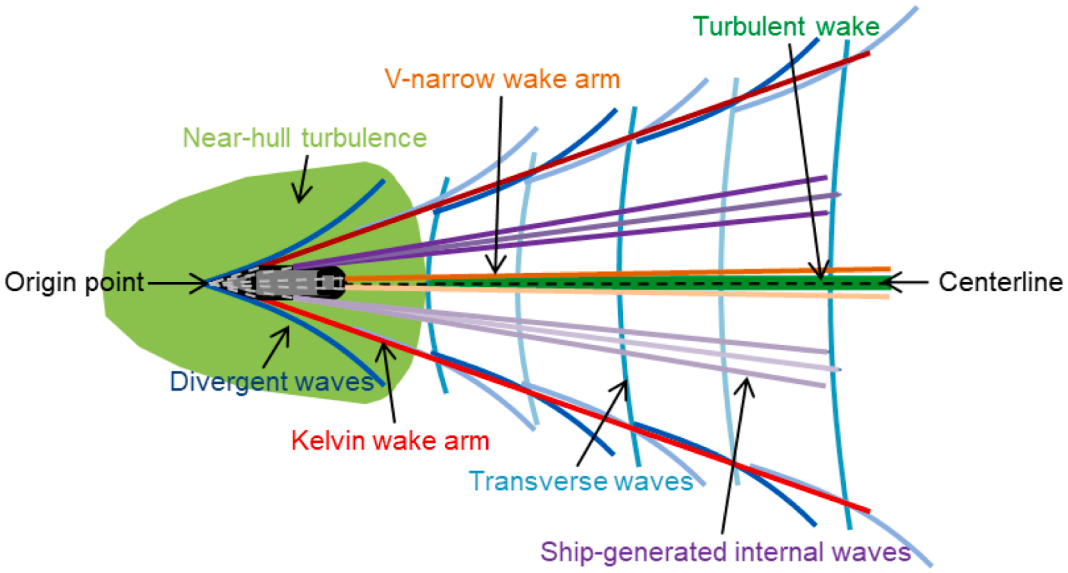

Fig. 1. Schematic representation of wake components detectable in SAR imagery (Tings, 2021).

- **Turbulent wakes** consist of two parts: the near field and the far field (Reed & Milgram, 2002). The near field normally refers to the rough ocean surface region a few ship lengths behind the ship. The far field describes the smooth ocean surface region, which sometimes is visible in SAR images a long time after the actual ship's passage, resulting in ocean surface anomalies up to hundreds of kilometers in length (Reed & Milgram, 2002; Milgram, et al., 1993). In this study, all kinds of rough ocean surfaces generated by the ship's movement and in the vicinity of the ship are considered as one wake component, which is here denoted as *near-hull turbulence* (NT). Besides the near field, near-hull turbulences also include turbulences imaged at the bow and at the side of a ship. As the predominantly visible part of the turbulent wake is actually the far field, in the following the term *turbulent wake* (TW) is only referring to the turbulent wake's far field, without the near field.
- **Kelvin wakes** also consist of multiple parts: typically, two wave systems with oscillating nature are generated by ships namely *divergent waves* and *transverse waves* (Darmon, et al., 2014; Rabaud & Moisy, 2013). In SAR those two wake components themselves are not frequently detectable (around 5 % of X-Band cases (Tings, 2021)), but distinct surface anomalies are imaged on a line of their constructive interference. These take the form of two bright lines with a V-like shape originating from the ship's bow or stern. While the term *Kelvin wake* combines all kinds of wake components belonging to the described pattern, in this study, only the two bright lines are considered as wake component and in the following are referred to by *Kelvin wake arms* (KW).
- **V–narrow wakes:** A V–shaped signature is also formed by the so-called *V–narrow wakes* (VW). V–narrow wakes consist of two bright lines with narrow angle close to the turbulent wake's region. Until today, the origin of the anomaly has not unambiguously been established and has a series of explanations (Zilman & Miloh, 1997). Independent from their origin of formation, V–narrow wakes are recognizable in SAR imagery due to the resulting Bragg scattering (Zilman & Miloh, 1997).
- **Internal waves** are not considered in this study, as they are encountered in SAR imagery only under rare conditions (below 1 % of X-Band cases (Tings, 2021)), mainly depending on the level of water stratification (Tunaley, et al., 1991; Hogan, et al., 1996; Wang, et al., 2017; Dysthe & Trulsen, 1989).

1.2. On comparison of detectability of ship wakes in SAR

By different SAR sensors, the wake components summarized in Fig. 1 can be detected with different probability (Tings, et al., 2020). As a glimpse Fig. 2 presents a collection of rare wake samples, where multiple wake components are imaged at once by four different SAR sensors. Several publications with focus on the comparison of ship wakes imaged by different SAR sensors can be found, but most of the published investigations only compare SAR sensors with frequency bands of significant differences in frequencies, e.g. L-Band wake signatures are often compared to C-Band or X–Band wake signatures, e.g. in (Alpers, et al., 1981; Lyden, et al., 1988; Milgram, et al., 1993; Oumansour, et al., 1996). Also, the publications only consider certain wake components and/or influencing parameters involved in the complex wave interaction, development and imaging of ship wakes. Therefore, instead of differences between C-Band and X–Band, some authors even conclude similarities, e.g. Milgram et at. with respect to wave attenuation and growth in the turbulent wake's region and the surrounding sea or Hennings et al. with respect to Kelvin wake arms (see next paragraph). However, it should be noted the only publications with focus on the detectability of ship wakes were previously published by the authors involved in this study (Tings & Velotto, 2018; Tings, et al., 2019; Tings, et al., 2020; Tings, 2021) and all other publications were only interpreted under this aspect, while their focus actually was not on detectability. Such interpretations of only a few publications reveal definite differences between X-Band and C-Band SAR sensors, i.e. Hennings et al. (Hennings, et al., 1999) and Gade et al. (Gade et al., 1998a, 1998b) as summarized in the next two paragraphs. Investigations of the effect of different slant ranges on the SAR imaging of ship wakes cannot be found in any published scientific studies.

Hennings et al. (Hennings, et al., 1999) compared Kelvin wake arms' signatures from L–Band, C–Band and X–Band SARs and simulated the relative mean Normalized Radar Cross Section (NRCS) of the cusp waves with respect to the background. They conclude that Kelvin wake arms are similarly detectable in C–Band as well as X–Band imagery and in contrast L–Band Kelvin wake arms are less distinctive from the background. Also, Gade et al. (Gade et al., 1998a, 1998b) compared SAR acquisitions between L-, C- and X–Band, showing that the dampening ratio of surface films increases with increasing radar frequencies. Turbulent wakes appear in SAR imagery due to ascending surfactants and bubbles after the ship's passage, which alter viscosity, temperature,

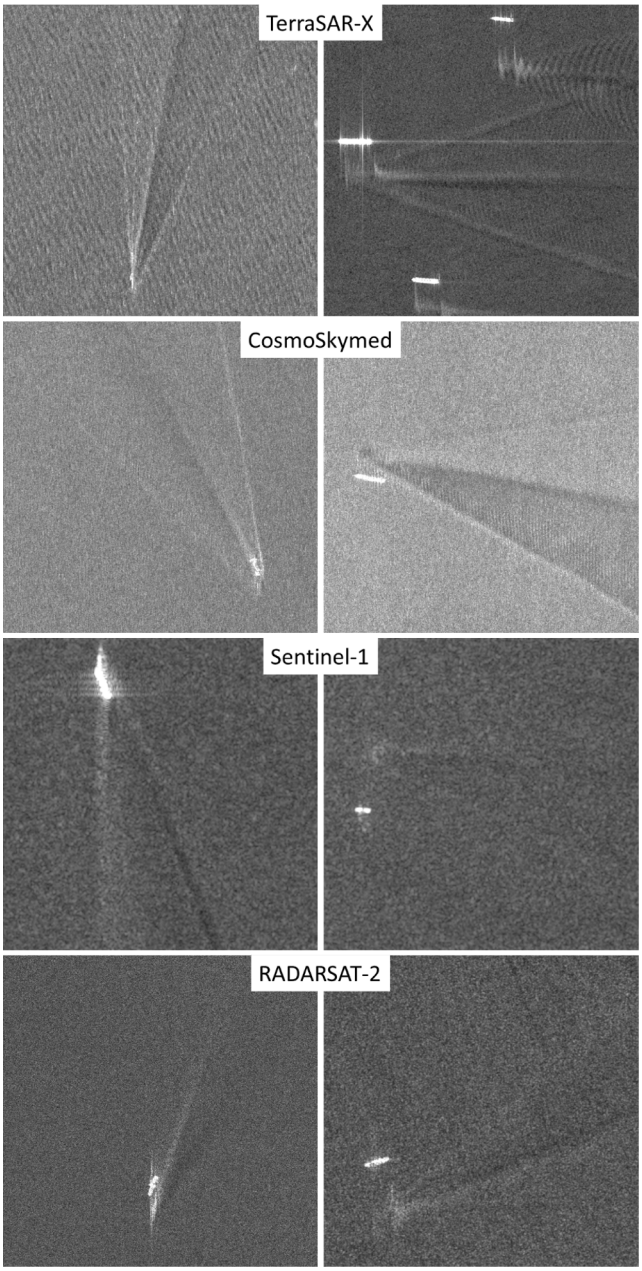

Fig. 2. Image collection of wakes from ships with movement directions roughly parallel to Azimuth (left column) or Range (right column) acquired by four different SAR missions.

surface tension and elasticity of the upper water layers (Soloviev, et al., 2010). These alterations result in a dampening of short surface waves visible in SAR in contrast to the background ocean surface (Pichel, et al., 2004). Therefore, the conclusions from Gade et al. (Gade et al., 1998a, 1998b) are here considered as analogy.

In (Tings & Velotto, 2018), the impact of different SAR sensors on the detectability of ship wakes was compared using three different SAR missions. It was summarized that ship wakes are better detectable in TerraSAR–X (TSX) data than in RADARSAT–2 (RS2) or Sentinel–1 (S1) data. The TSX satellites use X–Band–SAR sensors (Pitz & Miller, 2010) while RS2 and S1 use C-Band SAR sensors (Canadian Space Agency (CSA), 2019; European Space Agency (ESA), 2020). The other major difference between the three missions is the orbit altitude, which is much lower for TSX with 514 km (Pitz & Miller, 2010) compared to RS2 with 798 km (Canadian Space Agency (CSA), 2019) and S1 with 693 km (European Space Agency (ESA), 2020). Therefore, in (Tings & Velotto, 2018) could not be clarified if the orbit altitude or the radar frequency is responsible for the better detectability of ship wakes in TSX data.

Data from the CosmoSkymed (CSK) mission can be used as an additional dataset complementing the study setup of (Tings & Velotto, 2018). CSK satellites use X-Band SAR sensors and operate at 619 km (Italian Space Agency (ISA), 2007), an orbit altitude closer to S1 than to TSX. In (Tings, et al., 2020) a qualitative and quantitative comparison of the detectability of whole wake signatures between the four different sensors was conducted. The conclusion in (Tings, et al., 2020) is that the detectability between the four sensors is not comparable when ship wakes are considered as a whole, so the detectability of wake components should be considered individually.

1.3. Research questions

In this study, a comparison of detectability of the four individual wake components (near-hull turbulence (NT), turbulent wake (TW), Kelvin wake arms (KW) and V-narrow wakes (VW)) between the four sensors (TSX, CSK, RS2 and S1) is presented. In fact, environmental conditions, ship properties and image acquisition settings influence the detectable length of wake components in SAR imagery. The specific parameters describing physical conditions with influence on the detectable wake component length are denoted *influencing parameters*. The wake component length can be used as indicator for wake component detectability in dependency to those influencing parameters (Tings, 2021).

The distance between sensor and moving target directly influences the displacement of targets by Doppler effects in resulting SAR images. In this way, slant range plays a key role in nonlinearities in SAR imaging. Therefore, the focus in this paper is shifted from satellite orbit altitude to slant range R. Slant range can approximately be expressed as a function of orbit altitude h and incidence angle θ (McCandless & Jackson, 2004) by

$$R = h/\cos\theta \tag{1}$$

The motivation of this paper is to answer the two research questions:

RQ1 Are X-Band or C-Band missions better suited for the detection of ship wake components?
RQ2 Are shorter slant ranges or longer slant ranges better suited for the detection of ship wakes?

This paper presents the newest extended study on detectability of ship wakes and continues a series of preliminary investigations (Tings & Velotto, 2018; Tings, et al., 2019; Tings, et al., 2020; Tings, 2021) published before. Currently, this study and the sequence of previous studies are the only available publications with focus on detectability of ship wakes. The characteristics of influences on wake component detectability were concluded in (Tings, 2021), where for one SAR sensor with static orbit altitude also the influence of incidence angle was taken into account alongside a series of other influencing parameters. For multiple SAR sensors with different orbit altitude a missing differential point of view was recognized in (Tings, 2021). The intention of this study is to fill in this gap. Thus, one novelty of this study is the consideration of the impact of slant range on wake detectability, which is here considered solely and in combination to the two radar frequency bands: X–Band and C–Band. Another novelty is the explicit comparison of C-Band and X-Band SAR sensors, which operate frequency bands, which are often considered as having no significantly differentiating impact with respect to wake component detectability. Machine learning methods are used for comparison of wake component detectability.

2. Materials and method

In this section the used datasets are described. The applied method for detectability modeling is reviewed and the methods for detectability

Table 1
Properties of the manually generated wake datasets used in this study.

Sensor whole name	TerraSAR-X	CosmoSkymed	Sentinel-1	RADARSAT-2
Sensor name abbreviations in set *S*	TSX	CSK	S1	RS2
Frequency Band / radar wavelength [cm]	X / 3.1	X / 3.1	C / 5.6	C / 5.6
Orbit-Altitude [km]	514	619	693	798
Approx. slant range [km] at 30° / 50° incidence angle	593 / 800	715 / 963	800 / 1078	922 / 1242
Acquisition modes / product types	SL, SM / MGD	HIMAGE / DGM	IW / GRDH	MF, F, S / SGF
Number of total wake samples (HH / VV)	2692 (2273 / 419)	83 (83 / 0)	582 (0 / 582)	389 (389 / 0)
Proportion of no detected wake component [%]	21	17	29	41
Proportion of near-hull turbulences [%]	60	60	65	54
Proportion of turbulent wakes [%]	62	70	44	33
Proportion of Kelvin wake arms [%]	31	63	23	11
Proportion of V-narrow wake arms [%]	42	55	21	14

comparisons and estimation of uncertainties are introduced.

2.1. Data and parameters for detectability modeling

Table 1 summarizes the properties of the datasets acquired by the four spaceborne SAR sensors: TSX, CSK, S1 and RS2. Each wake sample in the datasets is the result of a manual inspection procedure, which was executed by the authors on thousands of SAR images to identify ocean surface areas where a ship wake must have been generated by a moving vessel. Only product types with projection to ground range are used. In detail, the executed manual inspection was as follows:

1. Intersection of SAR images with data from the Automatic Identification System (AIS) to locate all AIS–reported ship positions in the SAR images
2. Identification of candidate wake samples, i.e. all reported positions, where a minimum vessel velocity was reported
3. Filtering of all positive identifications containing SAR artifacts or anomalies not related to ship movements
4. Pre-processing of SAR images, i.e. radiometric calibration into NRCS, filtering of land and maritime objects and rescaling into uniform pixel spacing of 1.5 m per pixel
5. Selecting subimages from pre-processed SAR images with dimension of 5100 m in Azimuth and Range (3400 pixels each dimension)
6. Manual tracing of the four wake components (near-hull turbulence, turbulent wake, Kelvin wake arms, V-narrow wakes) in the subimages to build tracing vectors, which define the shape of each wake component by multiple image coordinates
7. Calculation of wake component lengths from the tracing vectors (zero means respective wake component is not detectable in the SAR image)

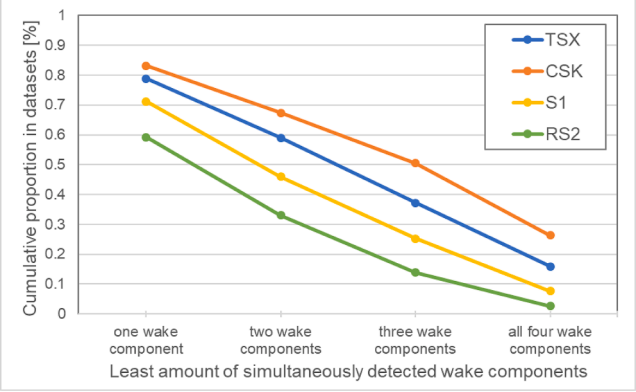

Fig. 3. Complementary Cumulative Distribution Function build for detected wake components for each satellite. For example, for RS2 at least one wake component was detected in ~ 59 % of cases, while all four wake components were detected simultaneously in ~ 3 % of cases. (For interpretation of the references to colour in this figure legend, the reader is referred to the web version of this article.)

The generated data used in the study for modelling detectability of wake components is made available to the public (Tings, 2022).

Fig. 3 provides a graphical overview of the proportion of candidate wake samples in each of the four sensor's datasets, where one or more wake components were detected simultaneously. The graphs present the Complementary Cumulative Distribution Function (CCDF) build for detected wake components for each satellite. CCDF is equal to "1-CDF" (Cumulative Distribution Function). For example, two wake components will be detected in ~ 67 % of all cases for CSK and only in ~ 33 % of all cases for RS2.

For this study, the influences are quantified by five influencing parameters, as introduced in Table 2. Note that instead of slant range the incidence angle is used for the modelling, as it implies a linear scaling of the parameter's value range, similar to the other influencing parameters, while the slant ranges over Range direction of the ground range projected image are scaling with $1/\cos\theta$. This facilitates the application of a linear model as motivated in the next subsection.

Table 2
List of the five influencing parameters with descriptions, value ranges and settings for numerical analysis of the five-dimensional feature space.

Nr x_i	Parameter name (units)	Description	Value range x_i^{min}	Value range x_i^{max}	Discrete bins $\boldsymbol{B}_i$	Bin count $\lvert B_i \rvert$
x_1	AIS-Vessel-Velocity (m/s)	Velocity of the vessel derived from AIS messages interpolated to the image acquisition time	1	10	$\{x_1 \in N \mid 1 \le x_1 \le 10\}$	10
x_2	AIS-Length (m)	Length of the corresponding vessel based on AIS information	5	35	$13, 20, 100, 200, 300$	5
x_3	AIS-CoG (degree)	The Course over Ground (CoG) based on AIS information relative to the radar looking direction (0° means parallel to range, 90° mean parallel to Azimuth).	0	90	$0, 15, 30, 45, 60, 75, 90$	7
x_4	Incidence-Angle (degree)	Incidence angle of the radar cropped to TSX's full performance value range	20	45	$\{x_4 \in N \mid 20 \le x_1 \le 45\}$	26
x_5	SAR-Wind-Speed (m/s)	Wind speed estimated from the SAR background around the vessel using the XMOD-2 (X–band) and CMOD-5 (C–band) geophysical model functions	2	9	$\{x_5 \in N \mid 2 \le x_1 \le 9\}$	8

2.2. Model function

The method for modelling and comparing wake component detectability is based on training a Support Vector Regression (SVR) model. Modelling wake component detectability by this method is adopted from (Tings, 2021). In the following, only a brief introduction to the method is provided, all details can be found in (Tings, 2021).

The setting of the SVR's hyperparameters is identical to (Tings, 2021), i.e. SVM–type is Epislon–SVR, Kernel-type is polynomial, Epsilon-loss is 0.001, Cost is 1.0 and Gamma is 0.0. Only the degree of the polynomial kernel is changed to first-degree polynomial. The reduction of the SVR's complexity is motivated in (Tings, 2021), where it was concluded that a second-degree polynomial would only be required for modelling the influence of AIS-CoG on the detectability of turbulent wakes. All other influences would be reproducible by the model, also when a first-degree polynomial is set. As the purpose of this study is the comparison of absolute wake component detectability between sensors, the error introduced by this simplification is irrelevant.

The model's complexity is reduced to increase robustness of the results, because the smaller dataset sizes used in this study facilitate overfitting. Here, robustness specifies the ability of the model to reproduce the same characteristics of influences on wake component detectability after additions and/or removals of data to the noisy training datasets were applied.

Each individual SVR model is trained for each wake component w for each sensor s, where $w \in W = \{NT, TW, KW, VW\}$ and $s \in S = \{TSX, CSK, RS2, S1\}$ resulting in 16 independently trained models. Input features to the SVR models are the five influencing parameters x_i. The models' prediction parameter (models' output) is the respective wake component's length $l_{w,s}$. It was calculated for the training data from the tracing vectors in the last step of the manual inspection procedure (see numeration in previous Subsection 2.1). This means, each SVR model $f_{w,s}$ learns the dependency between the influencing parameters and the wake component's length in the form:

$$l_{w,s} = f_{w,s}(x_1, \cdots, x_5) \tag{2}$$

2.3. Detectability comparison

When wake component's lengths are on average longer in the data of one sensor than in the data of another sensor, it can be assumed that the detectability of this wake component is for the one sensor higher than for the other sensor, which means the one sensor is better suited for the detection of this wake component. In order to make detectability of wake components comparable, the predicted wake component length $l_{w,s}$ needs to be converted to a measure of detectability with uniform scale. In (Tings, 2021) the so-called Detectable Length Metric (DLM) was introduced, which is adopted for this study. To obtain each $DLM_{w,s}$, each predicted value of wake component length is linearly normalized between the respective wake component's minimum length boundary l_w^{min} and maximum length boundary l_w^{max}, so that the unit of measurement [DLM] is a value between zero and one (0 = lowest detectability, 1 = highest detectability, linearly scaled) (i.e. $DLM_{w,s} \in [0, 1]$). $l_{w,s}$ is truncated to those boundaries before the calculation of results, but not for the calculation of uncertainties. The truncated $l_{w,s}$ is denoted $l'_{w,s}$ and $DLM_{w,s}$ is then calculated by the following formula:

$$DLM_{w,s}(l'_{w,s}) = (l'_{w,s} - l_w^{min}) / |l_w^{max} - l_w^{min}| \tag{3}$$

The applied settings for l_w^{min} and l_w^{max} in Table 3 are defined in (Tings, 2021) on the basis of percentiles.

In contrast to (Tings, 2021), in this work the detectability models are built for datasets of CSK, S1 and RS2, in addition to TSX. Due to the smaller size of the additional datasets the complexity of the detectability models is further reduced by only taking five influencing parameters into account. The reduction from nine to five influencing parameters is also established in (Tings, 2021).

For comparison between the sensors a uniform absolute measure of detectability is required. For this purpose, the average of $DLM_{w,s}(l'_{w,s})$ is calculated. The average $\overline{DLM_{w,s}}$ over the whole feature space can be calculated for each sensor s and wake component w by:

$$\overline{DLM_{w,s}} = \frac{1}{\Delta x_1 \cdots \Delta x_5} \int \cdots \int_V DLM_{w,s}(l'_{w,s})\, dx_1 \cdots dx_5 \tag{4}$$

where $\Delta x_i = x_i^{max} - x_i^{min}$ with $[x_i^{max}, x_i^{min}]$ as defined in Table 2. The multidimensional integration over the five-dimensional feature space is restricted by the volume $V = [x_1^{max}, x_1^{min}] \times \cdots \times [x_5^{max}, x_5^{min}] \subseteq \mathbb{R}^5$.

2.3.1. Uncertainty estimation

The original datasets are noisy with respect to the values of wake component length and of influencing parameters. The datasets are also unbalanced with respect to the distribution of samples over the value ranges, meaning some parts of the value range could have higher weighting. For this reason, comparing wake component lengths directly from the original datasets is not applicable. Each mean $\overline{DLM_{w,s}}$, as a result of integrating the models' prediction parameters, represents a mean wake component length from the input data balanced by a linear function over the five-dimensional feature space. Therefore, for comparing the detectability between sensors, $\overline{DLM_{w,s}}$ is calculated from the detectability models as being more appropriate.

The models still possess uncertainties, which have to be assessed when comparing the overall detectability by this method. The models' compositions are of interest in the conducted analyses, as they are designed to represent the characteristics of influences of influencing parameters on wake component detectability. This means, the model's degree of freedom is not optimized for estimating the measurements of wake component's lengths as they are included in the input datasets. Thus, those measurements cannot be applied for evaluating the models' performances, as they represent not the ground truth of the analyses. Consequentially, no metric of uncertainty requiring ground truth can be provided. The proposed method for uncertainty quantification evaluates, whether the models' compositions are learned systematically or randomly.

The following method provides not only means for analyzing uncertainty quantitatively, but also qualitatively: Each dataset is denoted $D_{w,s}$ and its number of wake samples is denoted $|D_{w,s}|$. Each $D_{w,s}$ is split into n subsets $D^j_{w,s}$ with its number of wake samples of $|D^j_{w,s}| = |D_{w,s}|/n$, where $j \in \{j \in \mathbb{N} | 1 \le j \le n\}$. The samples are systematically drawn from $D_{w,s}$ so that the five-dimensional feature space, spanned by the influencing parameters, is populated for each subset by samples distributed symmetrically over the parameters' value ranges. Then a detectability model $f^j_{w,s}$ is trained for each subset $D^j_{w,s}$.

As the learned SVR models are based on the first-degree polynomial kernel, they can be visualized mathematically by linear hyperplanes lying in a six-dimensional hyperspace (five influencing parameters plus wake component length). It is assumed in an ideal case (no manually introduced error, no unconsidered influences, etc.) with an infinite number of wake samples in all of the datasets that the linear hyperplanes trained for each of the n subsets $D^j_{w,s}$ would exactly superpose each other.

Table 3
Definitions of minimum length boundary and maximum length boundary for each wake component (in meters).

w	Wake component name	l_w^{min} [m]	l_w^{max} [m]
nt	Near-hull turbulence	0	200
tw	Turbulent wake	200	1250
kw	Kelvin wake arms	200	1500
vw	V-narrow wake arms	200	1750

This means, the distance between the planes in the direction of the $l_{w,s}$-dimension would be zero for any setting of the influencing parameters. In the non-ideal case of this study with a limited number of samples the deviations between the hyperplanes are used to express the uncertainty of the detectability model $f_{w,s}$.

Each of the models $f^{j}_{w,s}$ is contrasted against the respective other four models $f^{o}_{w,s}$ with $o \in \{o \in \mathbb{N} | 1 \leq o \leq n \bigwedge o \neq j\}$ resulting in m pairs of hyperplanes $\left(f^{j}_{w,s}, f^{o}_{w,s}\right)$. In order to quantify the deviation between each pair of hyperplanes, the influencing parameters are systematically sampled (B_i as defined in Table 2) and combined into a set of discrete model inputs. Then for all discrete model inputs the distances in the $l_{w,s}$-dimension are calculated for each pair of hyperplanes by:

$$\Delta f^{j,o}_{w,s}\left(x_{1,k_1}, \cdots, x_{5,k_5}\right) = f^{j}_{w,s}\left(x_{1,k_1}, \cdots, x_{5,k_5}\right) - f^{o}_{w,s}\left(x_{1,k_1}, \cdots, x_{5,k_5}\right)$$

$$\begin{aligned} &\forall j \in \{j \in \mathbb{N} | 1 \leq j \leq n\},\ \forall o \in \{o \in \mathbb{N} | 1 \leq o \leq n \bigwedge o \neq j\}, \\ &\forall k_i \in \{k_i \in \mathbb{N} | 1 \leq k_i \leq |B_i|\} \end{aligned} \tag{5}$$

Those distances $\Delta f^{j,o}_{w,s}$ are in the following called *intra-model-differences*. From these intra-model-differences, the root mean square error (RMSE) is calculated for each pair of hyperplanes $\left(f^{j}_{w,s}, f^{o}_{w,s}\right)$ by:

$$\mathrm{RMSE}^{j,o}_{w,s} = \sqrt{\frac{1}{|B_1| \cdots |B_5|} \sum_{k_1=1}^{|B_1|} \cdots \sum_{k_5=1}^{|B_5|} \left(\Delta f^{j,o}_{w,s}\left(x_{1,k_1}, \cdots, x_{5,k_5}\right)\right)^2}$$

$$\forall j \in \{j \in \mathbb{N} | 1 \leq j \leq 5\}, \forall o \in \{o \in \mathbb{N} | 1 \leq o \leq 5 \bigwedge o \neq j\} \tag{6}$$

The mean of $\mathrm{RMSE}^{j,o}_{w,s}$ over all m pairs then provides quantitative insight into the model's uncertainty:

$$\overline{RMSE_{w,s}} = \frac{1}{m} \sum_{j=1}^{n} \sum_{o=1, j \neq o}^{n, j \neq o} \mathrm{RMSE}^{j,o}_{w,s} \tag{7}$$

With $n = 5$ and $m = 20$ in this study the datasets are each split into five subsets and results in twenty pairs of hyperplanes being used for calculation of intra-model-differences and $\overline{RMSE_{w,s}}$. Further, for qualitative analysis, from all intra-model-differences normalized histograms are derived. The histograms are presented in Section 3.

2.3.2. Detectability comparison based on models

With an infinite number of wake samples in all datasets, the difference in detectability between the sensors could be depicted by the distance in the $l_{w,s}$-dimension between the hyperplanes. This means, when the hyperplane of one sensor with respect to $l_{w,s}$ on average lies above the hyperplane of another sensor, then the one sensor would have better wake detection performance.

Using the average $\overline{DLM_{w,s}}$ as calculated in (Eq. (4)) the mean difference of detectability between respectively-two sensors s_1 and s_2 can be determined by:

$$\overline{\Delta DLM_{w,s_1,s_2}} = \overline{DLM_{w,s_1}} - \overline{DLM_{w,s_2}} \tag{8}$$

In order to account for manually introduced error and unconsidered influences for our datasets with limited numbers of wake samples, all distances between all hyperplanes of one sensor $f^{j}_{w,s}$ to all hyperplanes of the other sensors $f^{j}_{w,t}$ with $t \in \{t \in S \bigwedge t \neq s\}$ within the volume V are collected. When using $n = 5$ hyperplanes for each of the two compared sensors, there are $\binom{5}{2} = 10$ combinations i.e. pairs of hyperplanes, from which the mean $\widehat{\overline{\Delta DLM_{w,s_1,s_2}}}$ is calculated. The procedure is similar to the calculation of the intra-model-differences for uncertainty estimation. Therefore, the collected distances are denoted *inter-model-differences* in the following.

For qualitative analysis, also for all inter-model-differences the histograms are derived and presented in Section 3 together with the intra-model-differences in the corresponding figures. For the calculation of $\widehat{\overline{\Delta DLM_{w,s_1,s_2}}}$ only the absolute differences between the hyperplanes are used (the algebraic sign does not play a role). However, to build the histograms of inter-model-differences, the differences between the hyperplanes are calculated in both directions (meaning from $f^{j}_{w,s}$ to $f^{j}_{w,t}$ and from $f^{j}_{w,t}$ to $f^{j}_{w,s}$). So, the histograms are symmetrical at the x-axis' origin.

2.3.3. Detectability comparison based on superimpositions of backscatter intensities

In addition to the analysis using the detectability models as basis (see Subsection 2.3.2), a redundant independent analysis based on the distribution of backscatter intensities in the wake components and in their surrounding is provided. Providing a redundant independent analysis reduces the possibility that the statements are originating from errors introduced during the manual tracing of wake components. For this redundant analysis, only an approximate position of the wake's origin point is required. Here, the wake's origin point from the manual inspection is used. For future analyses, it could also be gathered from automatic wake detection algorithms, as proposed in (Graziano, et al., 2016; Graziano, 2020). The results of this redundant analysis are presented in the discussion in case high uncertainty of the detectability models is encountered.

In order to create a uniform data basis, all images are rotated at the wake's origin points so that the ship's track is directed from left to right. A combination of ship heading and wake's centerline is used as basis for rotating the images. When rotated images are then superimposed with their respective wake's origin points in the center, then the individual wake components accumulated over all images are roughly lying on top of each other. The rotation is accomplished in three steps:

1. Polar transformation of the image into polar coordinate projection
2. Resampling of the polar transformed image in ascending angular order, beginning at the angle of the wake's centerline and ending at the angle before (phase unwrapping applied at the 360° to 0° switch)
3. Back transformation of the resampled image from polar coordinate system into Cartesian coordinate system.

Then all resampled, back transformed images are superimposed for accumulation of backscatter intensities. At the end, the accumulated intensities need to be divided by the amount of accumulations to obtain the original uniform scale of sigma naught values (NRCS). The superimpositions provide means for comparing the distinctiveness of wake signatures from ocean background between the sensors. Example superimpositions are shown in Fig. 4.

A set of such superimpositions $S_{w,s,k}$ are constructed for each wake component w, for each sensor s and for four data subsets k, which are defined in Table 4.

The four data subsets are extracted from each dataset of wake component w and sensor s. They are defined so that wake images contributing to a corresponding superimposition were acquired under similar ranges of influencing parameters. Incidence angles are converted to slant range to find matching ranges.

For better comparability, the information in the distribution of backscatter intensities of the superimpositions are condensed further so that the information can be plotted by curves into graphs, as follows:

1. The pixels $P_{\alpha,r}$ in the surrounding of the wake's origin point are assigned to one angular bin α and one radial bin r, where α and r are defined by angular and radial intervals fragmenting the region around the wake's origin point by $\alpha \in \{[\beta, \beta+1) | \forall \beta \in \mathbb{N}, 0 \leq \beta \leq 359\}$ (in degree) and $r \in [[0, 200), [200, 400), [400, 800), [400, 1600), [1600, 3200)]$ (in meters).

The mean over all $|P_{\alpha,r}|$ intensities of pixels $P_{\alpha,r}$ is calculated for each superimposition $S_{w,s,k}$:

$$\overline{S_{w,s,k}}(\alpha, r) = \frac{1}{|P_{\alpha,r}|} \sum_{p \in P_{\alpha,r}} S_{w,s,k}(p) \tag{9}$$

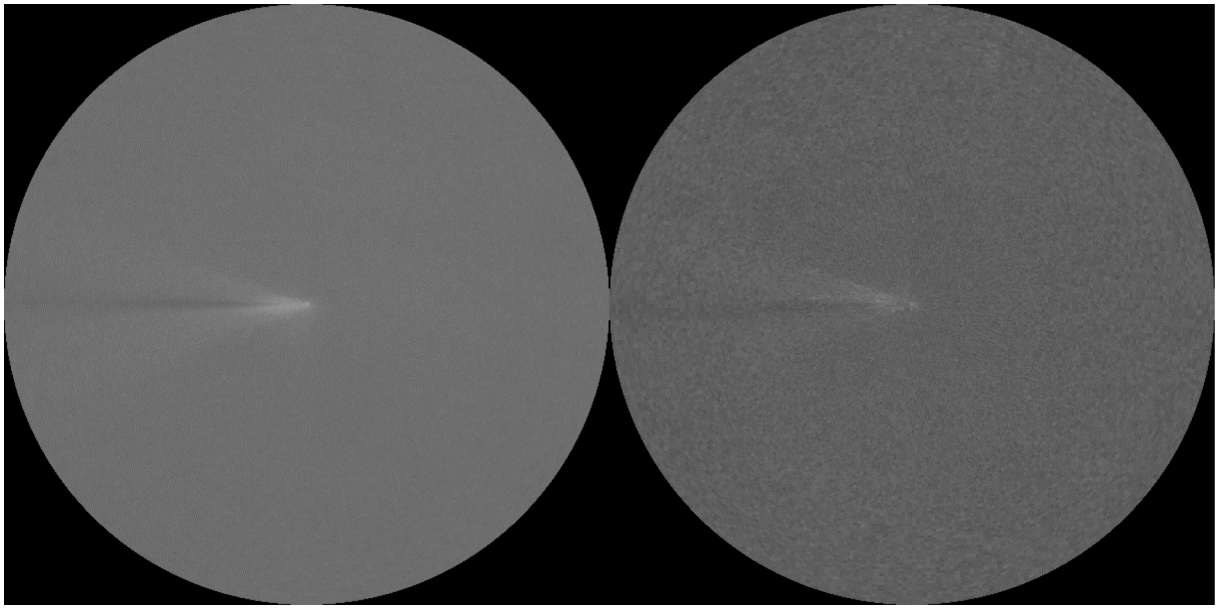

Fig. 4. Examples of superimpositions of wake samples containing turbulent wakes acquired under short slant ranges by TSX (left) and CSK (right).

Table 4
Definition of data (sub)sets for superimposition of backscatter intensities.

Dataset index k	Slant ranges	Incidence angle
1	Shortest ranges of each sensor	20° to 30°
2	Medium ranges of each sensor	30° to 40°
3	Longest ranges of each sensor	40° to 50°
4	TSX: 700 m to 750 *m* CSK: 675 m to 800 *m* S1: 800 m to 850 *m* RS2: 900 m to 1000 *m*	Variable to achieve matching slant ranges:

3. For each radial bin one curve is then plotted for each superimposition $S_{w,s,k}$, with the angular bins α on the x-axis and the mean intensity $\overline{S_{w,s,k}}(\alpha, r)$ on the y-axis. The angular bin $\alpha = 0$ marks the position of the wake's centerline.

While those graphs in the Figs. 10 to 13 constitute a qualitative analysis, they are accompanied by calculations of ratios of clutters' and wake component's mean intensity for quantitative analysis. The ratios for each dataset i are calculated as follows:

1. The intensity values of all background pixels are collected for each sensor s into set $I_{clutter,s,k}$
2. The intensity values of all pixels of each wake component w are collected for each sensor s into set $I_{w,s,k}$
3. Mean clutter intensities $\mu_{clutter,s,k}$ are calculated for the sets $I_{clutter,s,k}$ and mean wake component intensities $\mu_{w,s,k}$ are calculated for the sets $I_{w,s,k}$
4. Ratios of clutter's and wake component's mean intensity are determined by:

$$q_{w,s,k} = \mu_{w,s,k} / \mu_{clutter,s,k} \tag{10}$$

It should be noted that pixels were extensively discarded from calculations by introducing a buffer area around the wakes as a combination of all detected wake components and by filtering invalid regions like land or ship signatures.

3. Results

In the following, the comparison of detectability between the four satellite missions for the four ship wake components are presented. The sensor specific measurements are presented in sensor specific colors, i.e. TSX in blue, CSK in orange, RS2 in green and S1 in yellow. (For interpretation of the colour in the figures, the reader is referred to the web version of this article.) The results for each wake component are depicted in individual Figures:

- near–hull turbulences (Fig. 5(a) and Fig. 6)
- turbulent wakes (Fig. 5(b) and Fig. 7)
- Kelvin wake arms (Fig. 5(c) and Fig. 8)
- V–narrow wakes (Fig. 5(d) and Fig. 9)

In Fig. 5 the model derived information is depicted for each sensor s by accordingly colored bars and for each wake component w in a dedicated plot numbered from (a) to (d), respectively. The X–Band sensors TSX and CSK are located on the left side in the plots and the C–Band sensors to the right side. Also, in the plots the sensors are sorted in ascending order from left to right according to their orbit altitudes, e.g. RS2 has the longest slant ranges and TSX the shortest. The plots show the calculated means $\overline{DLM_{w,s}}$. For comparison to the respective other sensors, the calculated $\overline{\Delta\widehat{DLM}_{w,s_1,s_2}}$ are added to $\overline{DLM_{w,s}}$ and the respective offsets are indicated by colored symbols, which are unique for each sensor. In the figures, also $\overline{RMSE_{w,s}}$ is visualized for each sensor in the form of an error bar. In fact, the differences $\overline{\Delta\widehat{DLM}_{w,s_1,s_2}}$ are identical, so drawing all symbols of the summations of $\overline{DLM_{w,s}}$ with $\overline{\Delta\widehat{DLM}_{w,s_1,s_2}}$ for each sensor is redundant. However, the plots were designed in that way so that the $\overline{RMSE_{w,s}}$ error bars can be plotted for each $\overline{DLM_{w,s}}$ in relation to $\overline{DLM_{w,s}}$ and $\overline{\Delta\widehat{DLM}_{w,s_1,s_2}}$.

From initial evaluation of these results can be recognized:

- that both C-Band sensors reach lower DLMs for most wake components than X-Band sensors
- that the sensor with longest slant ranges, i.e. RS2, is the sensor with lowest DLMs for all wake components.

Based on this first guess, the next section discusses the main questions of this study, which were defined in the introduction section.

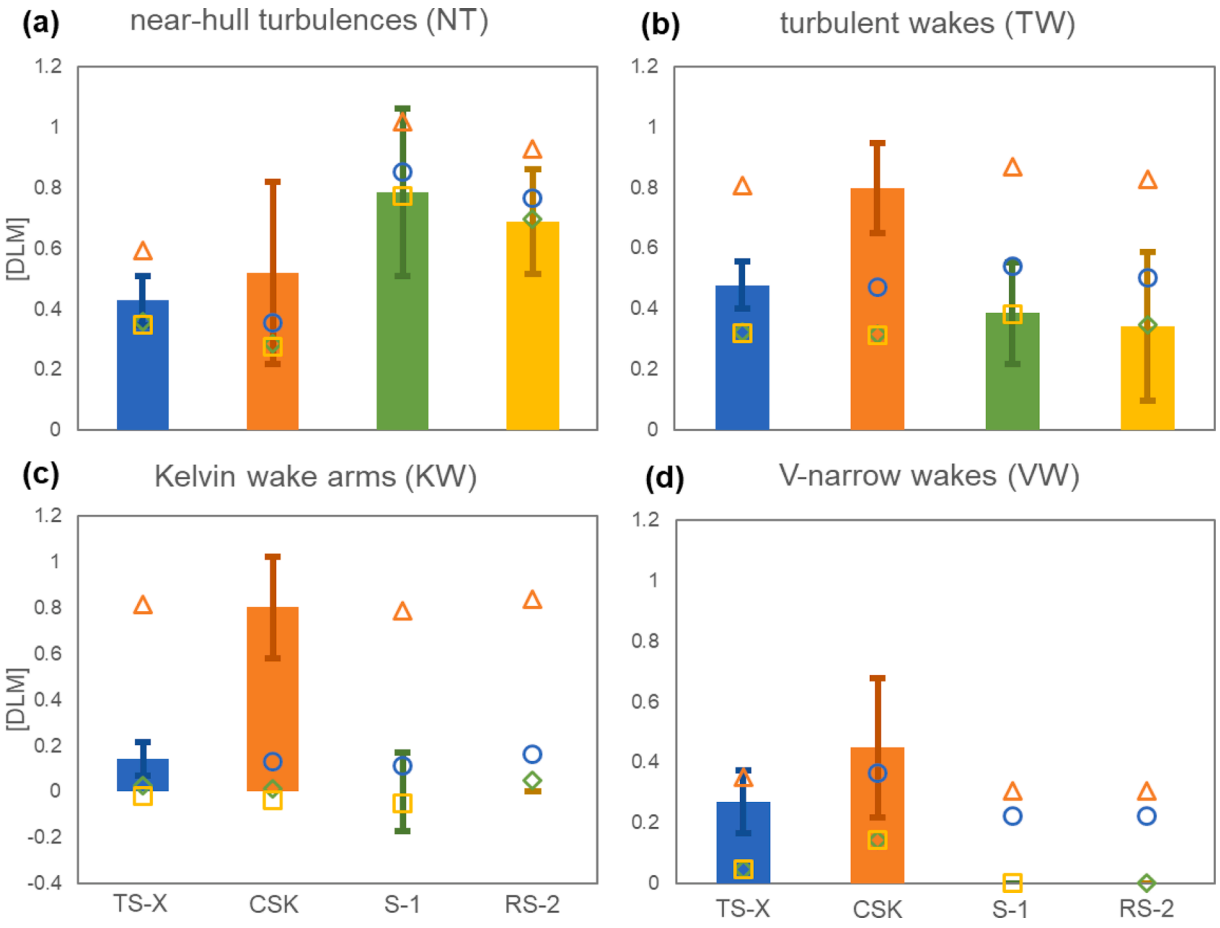

Fig. 5. Results of $\overline{DLM_{w,s}}$, $\overline{RMSE_{w,s}}$ and the relative representations of $\overline{\widehat{\Delta DLM_{w,s_1,s_2}}}$. The vertical axis is labelled by [DLM] as the thee variables $\overline{DLM_{w,s}}$, $\overline{RMSE_{w,s}}$, $\overline{\widehat{\Delta DLM_{w,s_1,s_2}}}$ are measurements in the scale of this unit. In case the bars are not visible in the plots, this means $\overline{DLM_{w,s}} = 0$. The calculated $\overline{\widehat{\Delta DLM_{w,s_1,s_2}}}$ are added to $\overline{DLM_{w,s}}$ and the respective offsets are indicated by colored symbols, which are unique for each sensor. $\overline{RMSE_{w,s}}$ is visualized for each sensor in the form of an error bar. (For interpretation of the references to colour in this figure, the reader is referred to the web version of this article.)

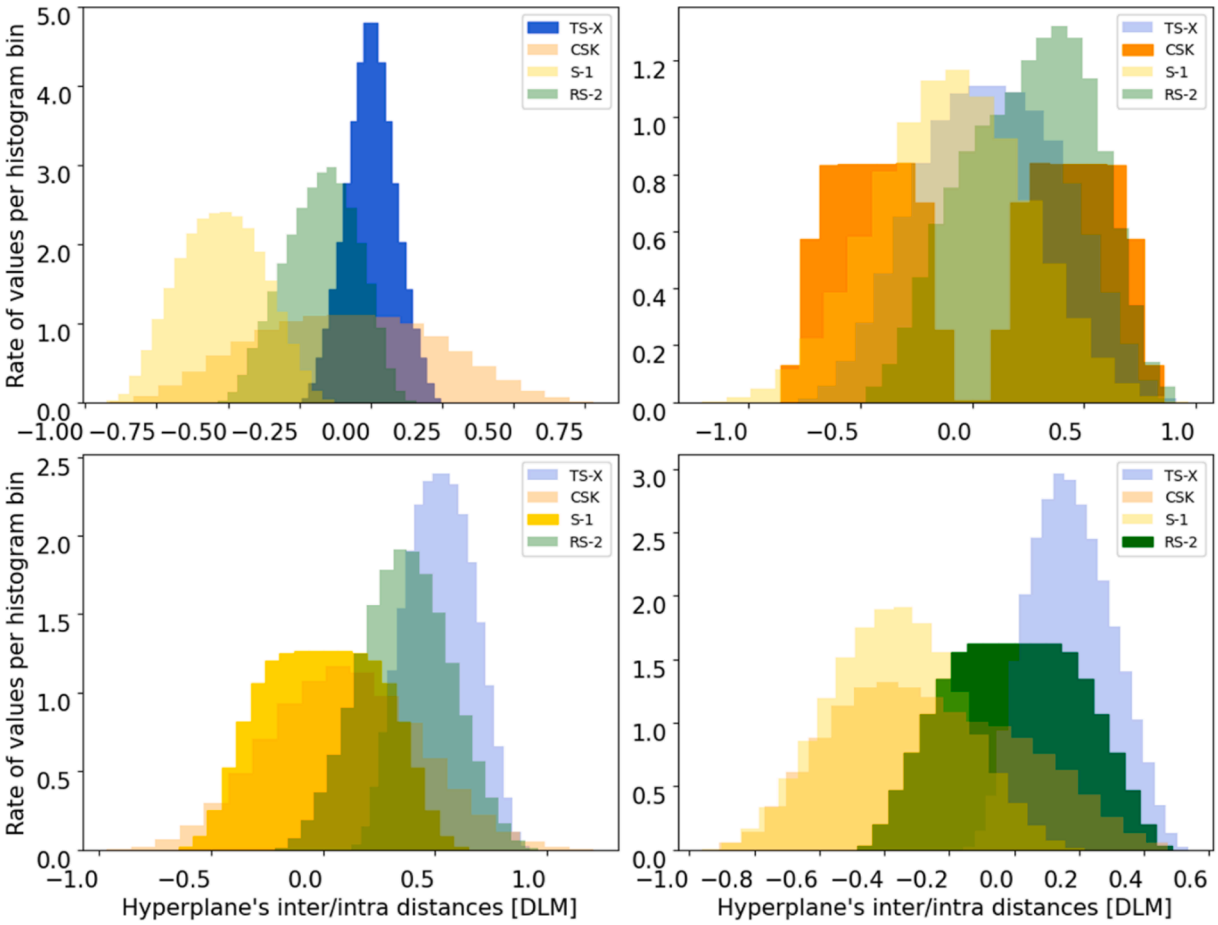

Fig. 6. Histograms of intra-model-differences and inter-model-differences for near-hull turbulences. (For interpretation of the references to colour in this figure legend, the reader is referred to the web version of this article.)

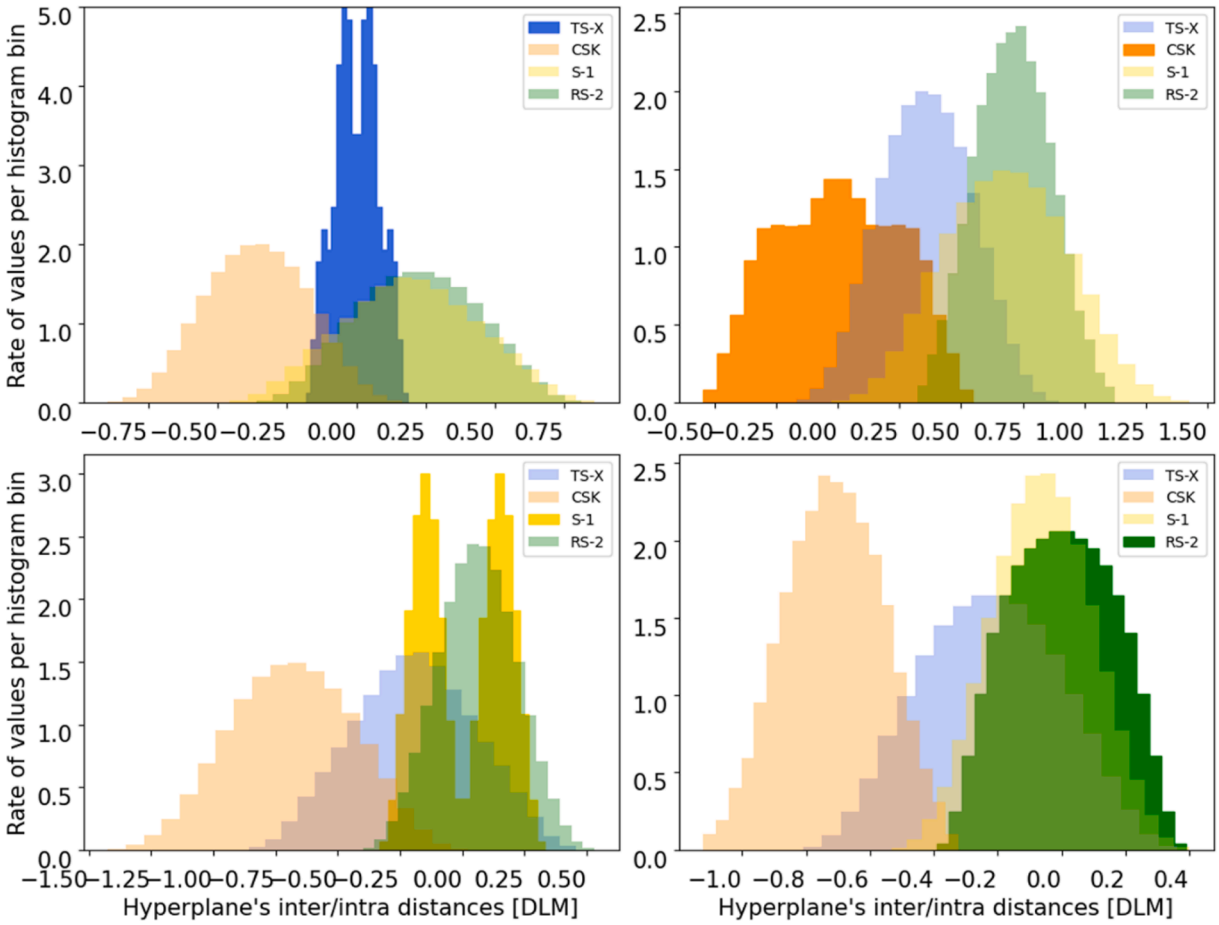

Fig. 7. Histograms of intra-model-differences and inter-model-differences for turbulent wakes. (For interpretation of the references to colour in this figure legend, the reader is referred to the web version of this article.)

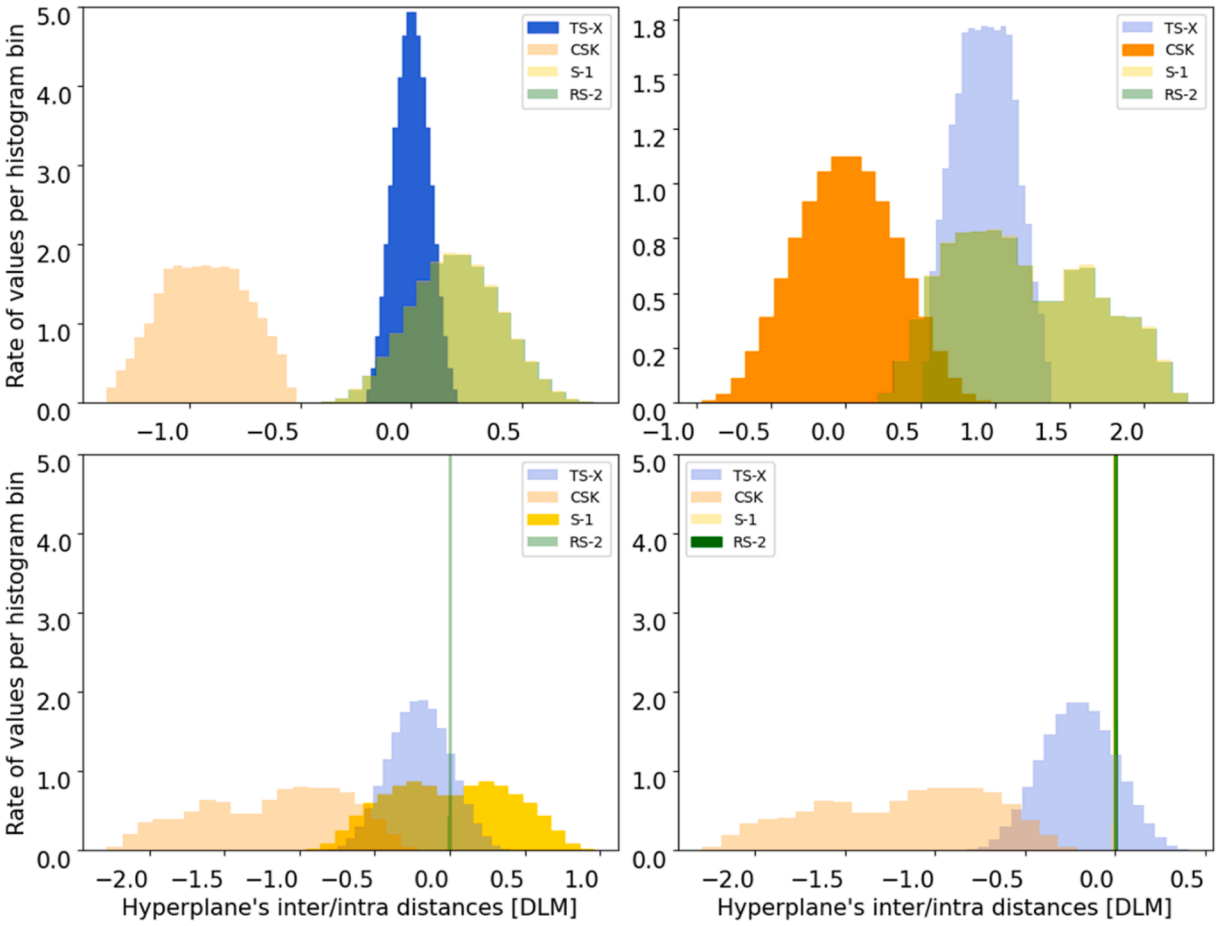

Fig. 8. Histograms of intra-model-differences and inter-model-differences for for Kelvin wake arms. (For interpretation of the references to colour in this figure legend, the reader is referred to the web version of this article.)

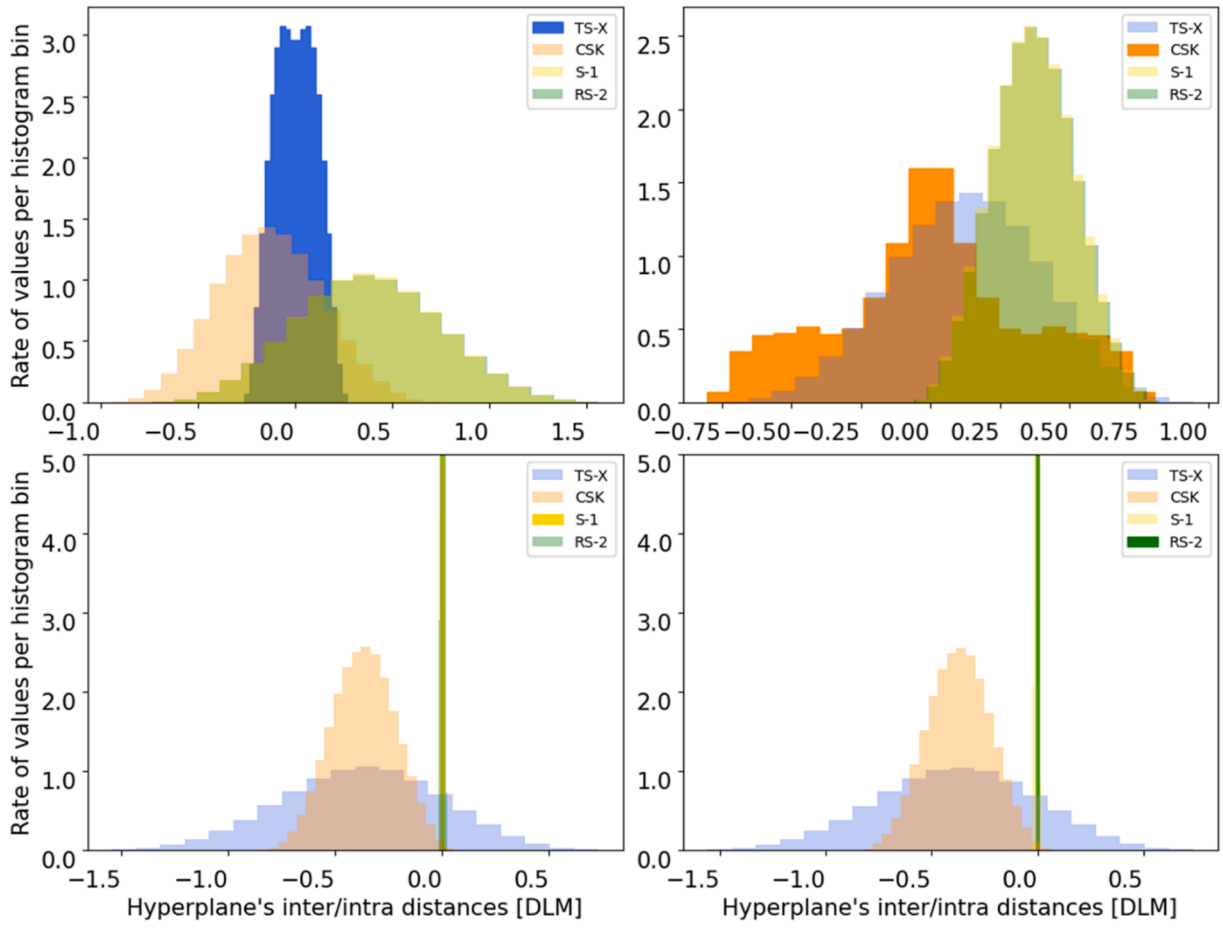

Fig. 9. Histograms of intra-model-differences and inter-model-differences for V-narrow wakes. (For interpretation of the references to colour in this figure legend, the reader is referred to the web version of this article.)

In the Figs. 6 to 9, for each sensor and each wake component, the histogram of intra-model-differences and the corresponding three other histograms of inter-model-differences are presented for each wake component in one graph. In each graph the histogram of intra-model-differences is depicted by solid bars in the respective sensor's color and the corresponding other three inter-model-differences are depicted by transparent bars in the respective other three sensors' colors. This means, with the four compared sensors, for each wake component four graphs each with four histograms are shown in Figs. 6 to 9. It should be noted that the histograms of intra-model-differences are symmetric to the x-axis's origin, because $\Delta f^{j,o}_{w,s}$ estimate non-absolute values and for each $\Delta f^{j,o}_{w,s}$ the counterpart $\Delta f^{o,j}_{w,s}$ exists. The graphs can be considered for a deeper understanding of the connection between $\overline{RMSE_{w,s}}$, $\overline{DLM_{w,s}}$ and $\overline{\widehat{\Delta DLM}_{w,s_1,s_2}}$ and are referred to in the discussion in the next section.

4. Discussion

The dependency of detectability of individual wake components on radar frequencies and/or slant ranges is studied qualitatively and quantitatively. For all pairs of sensors, the significance of differences in detectability is determined. Quantitatively the differences $\overline{\widehat{\Delta DLM}_{w,s_1,s_2}}$ and uncertainties $\overline{RMSE_{w,s}}$ in Fig. 5 are contrasted and qualitatively the histograms of intra-model-differences and inter-model-differences in Figs. 6 to 9 are interpreted.

As additional indicator for wake detectability, the image contrast between ocean background and wake affected area from the superimpositions of backscatter intensities accumulated over data subsets is used and also the ratios of clutter's mean intensity to wake component's mean intensity are considered. These redundant independent analyses are added for reviewing significance of conclusions about differences in detectability. The respective Figs. 10 to 13 are shown in the flow of discussion below.

It is essential to consider the model's uncertainty of both sensors, when contrasting $\overline{\widehat{\Delta DLM}_{w,s_1,s_2}}$ with $\overline{RMSE_{w,s}}$ during the quantitative analysis. When only one of the two $\overline{RMSE_{w,s_1}}$ or $\overline{RMSE_{w,s_2}}$ is higher than $\overline{\widehat{\Delta DLM}_{w,s_1,s_2}}$, then difference in detectability can be considered as insignificant. The elevation of $\overline{DLM_{w,s_1}}$ of one sensor s_1 over $\overline{DLM_{w,s_2}}$ of the other sensor s_2 can only be considered as significant when $\overline{RMSE_{w,s_1}} < \overline{\widehat{\Delta DLM}_{w,s_1,s_2}}$ and $\overline{RMSE_{w,s_2}} < \overline{\widehat{\Delta DLM}_{w,s_1,s_2}}$.

The following also holds for each wake component w: when the peaks of a histogram of inter-model-differences of sensor s_1 are located between two peaks of the histogram of intra-model-differences of sensor s_2, then the hyperplanes trained for the five subsets X'^{j}_{w,s_2} have in total larger distances to each other than to the hyperplanes trained for the five subsets X^{j}_{w,s_1}. This means, the model's uncertainty is higher than the differences in detectability between s_1 and s_2. So, by qualitative analysis the model's uncertainty renders statements on differences insignificant. Insignificance by qualitative analysis can also be indicated when histograms of intra-model-differences and inter-model-differences can visually not intuitively be separated from each other, i.e. they show a strong overlap between each other.

In the following, the two principal research questions RQ1 and RQ2 as defined in Subsection 1.3 are discussed. Each question will be

discussed in a separate subsection. In the Subsections 4.1 and 4.2, explanations are provided for each wake component separately at first and then followed by a general conclusion. Finally, all results are summarized by Table 5 in Subsection 4.3.

4.1. Comparison of detectability between X-Band and C-Band SAR sensors

In this subsection the research question RQ1 is discussed, separately for each wake component in 4.1.1 to 4.1.4 and generally in 4.1.5.

4.1.1. Comparison of X-Band with C-Band with respect to detectability of near-hull turbulences

The need for estimating the models' uncertainties becomes most evident here. In fact, Fig. 5(a) shows that $\overline{DLM_{NT,S1}} > \overline{DLM_{NT,RS2}} > \overline{DLM_{NT,CSK}} > \overline{DLM_{NT,TSX}}$. So, by only considering $\overline{DLM_{NT,s}}$ the postulation could be derived that C–Band would even perform better than X–Band on the detection of near–hull turbulences. But, the respective model's uncertainties $\overline{RMSE_{NT,s}}$ are highest for this wake component. $\overline{RMSE_{NT,s}}$ is larger than most $\overline{\Delta\widehat{DLM}_{NT,s_1,s_2}}$ differences, except for the two cases $\overline{RMSE_{NT,TSX}} < \overline{\Delta\widehat{DLM}_{NT,TSX,CSK}}$ and $\overline{RMSE_{NT,RS2}} < \overline{\Delta\widehat{DLM}_{NT,RS2,CSK}}$, where the uncertainties of the TSX and the RS2 models are lower than the mean differences of detectability towards CSK. Conversely, the uncertainty of the CSK model is higher than the mean differences of detectability towards the other three sensors: $\overline{RMSE_{NT,CSK}} > \overline{\Delta\widehat{DLM}_{NT,CSK,s_n}}$, $\forall s_n \in \{TSX, S1, RS2\}$. So, none of the differences $\overline{\Delta\widehat{DLM}_{NT,s_1,s_2}}$ are considered significant.

This insignificance is also indicated by the histograms of intra-model-differences and inter-model-differences in Fig. 6. It can be recognized in Fig. 6 that the histogram of intra-model-differences for CSK (solid orange histogram) shows two peaks symmetric to the x-axis' origin. The histograms of the other three sensors are located between those peaks. This means, by qualitative analysis the differences in detectability of near-hull turbulences between CSK and each TSX, RS2 as well as S1 are not significant with respect to the model's uncertainty. Fig. 6 also shows that histograms of TSX and RS2 intra- and inter-model-differences are overlapping with more than ~ 50 % of the histogram's areas. As the histogram curves cannot be separated from one another, the offsets $\overline{\Delta\widehat{DLM}_{NT,TSX,RS2}}$ and $\overline{\Delta\widehat{DLM}_{NT,RS2,TSX}}$ from $\overline{DLM_{NT,TSX}}$ with $\overline{RMSE_{NT,TSX}}$ and $\overline{DLM_{NT,RS2}}$ with $\overline{RMSE_{NT,RS2}}$, respectively, are not considered significant. For completeness, it should be noted that the histograms of TSX and S1 are visually separable. So, by qualitative analysis of the detectability models TSX would be better suited for detecting near-hull turbulences than S1, but this was already discarded as explained in the previous paragraph.

In order to answer the question for TSX and S1 also qualitatively with the alternative analysis, Fig. 10 is considered: Although the general magnitude of mean backscatter intensities differs significantly between the sensors, a contrast between the wake's centerline (at 0° on the x-axis) and the ocean background can only be observed until the 800 m wake length bins. The higher variability of mean backscatter intensities of the CSK, RS2 and S1 graphs reflects the higher model's uncertainty indicated by the respective intra-model-differences in Fig. 6 as well as $\overline{RMSE_{NT,CSK}}$, $\overline{RMSE_{NT,S1}}$ and $\overline{RMSE_{NT,RS2}}$, which is highest for CSK. The graphs in Fig. 10 for TSX and S1 show maxima with similar relative heights at the position of the wake's centerline for the range bins 200 m, 400 m and 800 m. This means, for both sensors near-hull turbulences only produce higher ocean backscatter contrasting from the ocean background up to 800 m aft the ship. Therefore, no significant difference in detectability between TSX and S1 is also concluded by the alternative

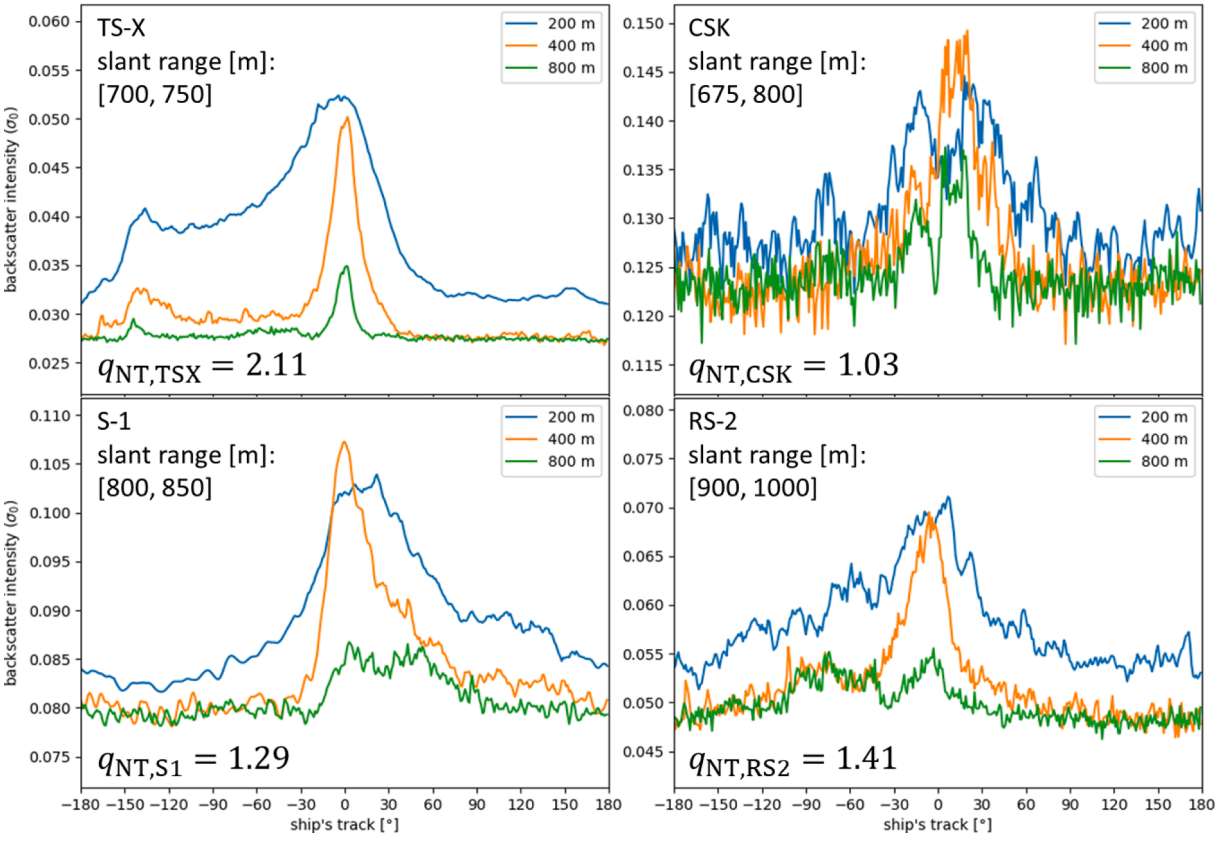

Fig. 10. Distribution of mean backscatter intensities of superimpositions based on matching slant ranges for near-hull turbulences. (For interpretation of the references to colour in this figure legend, the reader is referred to the web version of this article.)

qualitative analysis. With respect to Fig. 10 also no significant difference can be recognized between the other sensors. The slant ranges are set to matching value ranges for all four sensors. Thus, it can be ruled out that a better detectability of near–hull turbulences in C-Band than in X-Band imagery is not recognizable due to a compensation of the nonlinear decrease of detectability with increasing slant ranges.

This conclusion is also supported by the quantitative alternative analysis with the ratios of clutter's and near-hull turbulences' mean intensity $q_{NT,s}$ also shown in Fig. 10, from which no trend can be derived: The ratios are highest for TSX and second highest for RS2, while $q_{NT,CSK}$ reveal that relative backscatter of near-hull turbulences is only little higher in contrast to the ocean background.

4.1.2. Comparison of X-Band with C-Band with respect to detectability of turbulent wakes

Taking the studies of Gade et al. (Gade et al., 1998a, 1998b) as analogy for turbulent wakes would imply that due to higher damping ratio of surface films in X–Band imagery in comparison to C–Band imagery, turbulent wakes should be better detectable in X–Band imagery. Indeed, the results in Fig. 5(b) show ~ 9 % higher $\overline{DLM_{TW,TSX}}$ for TSX and even ~ 31 % higher $\overline{DLM_{TW,CSK}}$ for CSK in contrast to RS2 and S1, which have similar $\overline{DLM_{TW,s}}$ (only ~ 4 % distance), i.e. $\overline{DLM_{TW,CSK}} \gg \overline{DLM_{TW,TSX}} > \overline{DLM_{TW,S1}} \gtrsim \overline{DLM_{TW,RS2}}$.

However, when taking $\overline{RMSE_{TW,s}}$ or the histograms of intra-model-differences and inter-model-differences in the Fig. 7 into account, by quantitative and qualitative uncertainty analysis the elevation of $\overline{DLM_{TW,TSX}}$ over $\overline{DLM_{TW,RS2}}$ and $\overline{DLM_{TW,S1}}$ is not significant: $\overline{RMSE_{TW,S1}} > \overline{\widehat{\Delta DLM_{TW,S1,TSX}}}$, $\overline{RMSE_{TW,RS2}} > \overline{\widehat{\Delta DLM_{TW,RS2,TSX}}}$ and the respective histograms of intra- and inter-model-differences are overlapping with more than ~ 50 % of the histogram's areas. Therefore, it can be concluded that CSK is indeed better suited for the detection of turbulent wakes than RS2 and S1 ($\overline{RMSE_{TW,CSK}} < \overline{\widehat{\Delta DLM_{TW,CSK,s_n}}}$, $\forall s_n \in \{TSX, S1, RS2\}$ and $\overline{RMSE_{TW,s_n}} < \overline{\widehat{\Delta DLM_{TW,s_n,CSK}}}$, $\forall s_n \in \{TSX, S1, RS2\}$), but not that X–Band is better suited than C–Band.

This conclusion can mainly be confirmed by the alternative consideration of the mean backscatter intensities as depicted in Fig. 11. No significant difference of minimum backscatter intensities at the wake's centerline angle with 800 m to 3200 m distance to the wake's origin point is recognizable between TSX and S1. In RS2 turbulent wake signatures are rarely encountered above 800 m distance. That RS2 might have lower performance than TSX and S1 is not indicated by the quantitative and qualitative analysis of the detectability models and therefore neglected. The minimum at the wake's centerline for CSK (highlighted in Fig. 11 by the red ellipsis) show significantly higher local contrast in comparison to the other three sensors. The expected characteristic pattern of turbulent wakes (i.e. low radar backscatter sometimes enclosed by brighter backscatter due to Kelvin wake arms) is clearly recognizable. This indicates that in CSK images the ocean surface smoothed by the turbulent wake is better observable than in imagery from the other sensors. Again, the plots were generated for matching slant ranges so that the impact of varying slant ranges between the sensors is compensated.

Also, for turbulent wakes the quantitative alternative analysis does not show clear similarities or differences between C-Band and X-Band sensors. Furthermore, the better performance of CSK cannot be confirmed by the quantitative alternative analysis.

4.1.3. Comparison of X-Band with C-Band with respect to detectability of Kelvin wake arms

The $\overline{DLM_{KW,RS2}} \approx \overline{DLM_{KW,S1}} \approx 0$ and its low $\overline{RMSE_{KW,RS2}}$ as indicated

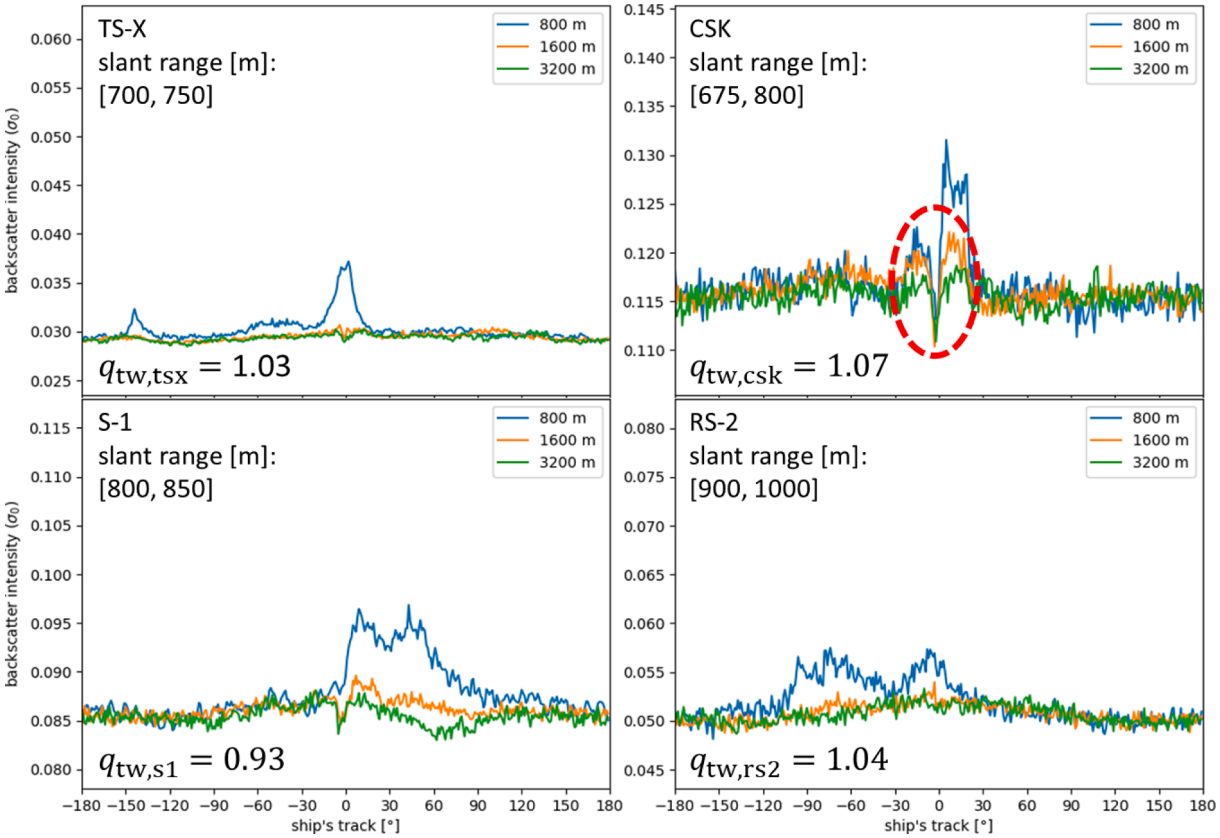

Fig. 11. Distribution of mean backscatter intensities of superimpositions based on matching slant ranges for turbulent wakes; the curves for the 200 m and 400 m radial bins are not displayed; the red ellipsis marks the minimum NRCS at the wake's centerline. (For interpretation of the references to colour in this figure legend, the reader is referred to the web version of this article.)

in Fig. 5, imply that almost all RS2 and S1 wake samples did show no or only very short signatures of those wake components. The corresponding detectability models represent hyperplanes with low elevation in the $l_{w,s}$-dimension. However, with higher $\overline{RMSE_{KW,S1}} > 0.2$ the previous implication does not hold for Kelvin wake arms in S1 imagery. As $\overline{RMSE_{KW,S1}} > \overline{\Delta\widehat{DLM}_{KW,S1,TSX}}$ TSX cannot be considered significantly better suited for detection of Kelvin wake arms than S1. With $\overline{RMSE_{KW,RS2}} < \overline{\Delta\widehat{DLM}_{KW,RS2,s_n}}, \forall s_n \in \{TSX, CSK\}$ and $\overline{RMSE_{KW,s_n}} < \overline{\Delta\widehat{DLM}_{KW,s_n,RS2}}, \forall s_n \in \{TSX, CSK\}$ TSX and CSK are significantly better suited than RS2. It should be noted that CSK does outperform all other sensors.

The histogram of intra-model-differences of TSX is visually separable from the histograms of inter-model-differences of S1 and RS2. Vice versa the histogram of inter-model-differences of TSX is only separable from the histogram of intra-model-differences of RS2 not of S1 (as presented in Fig. 8). Both histograms of CSK are can be separated from all other histograms. This implies that all statements from the quantitative analysis can be confirmed by the qualitative analysis of the detectability models. Basically, this conclusion agrees with Hennings et al. (Hennings, et al., 1999) stating that C–Band or X–Band should be similar in terms of detectability of Kelvin wake arms. However, in Hennings et al. only the mean NRCS of the Kelvin wake arms relative to the background was taken into account, the wake component length was not considered. Nevertheless, it can be seen in the Figures in (Hennings, et al., 1999) that the Kelvin wake arms are longer for X–Band than for C–Band imagery. Further, the better detectability of Kelvin wake arms in higher frequency SARs (in (Hennings, et al., 1999) C-Band and X-Band) compared to lower frequency SARs (in (Hennings, et al., 1999) L-Band) could analogically apply for the difference in detectability between C-Band and X-Band SARs as well, because C–Band means lower frequencies than X–Band.

The alternative analysis of the mean backscatter intensities reveals that the characteristic Kelvin wake pattern consisting of two bright lines with 19.47° angle from the wake's centerline is essentially observable under such low incidence angles or analogically short slant ranges, as they are only reached by the two X-Band sensors (as depicted in Fig. 12). For incidence angles above 30° the characteristic Kelvin wake pattern is not as dominant as under lower incidence angles. However, it is still recognizable for TSX, CSK and even for S1 (see Fig. 13), but not for RS2. As RS2 has the longest slant ranges of all four sensors and Kelvin wakes are not found significantly lower detectable in S1 imagery, the difference in detectability is attributed to the different slant ranges of the sensors, not to the different radar frequencies.

By the quantitative alternative analysis this statement can be confirmed. The longer the slant ranges become the closer the ratios of clutter's and Kelvin wake arm's mean intensity converge to one. This means, under shorter slant ranges the cusp waves in the Kelvin wake arms produce higher backscatter relative to the background clutter in contrast to the cusp waves under longer slant ranges, which makes Kelvin wake arms under shorter slant ranges better detectable.

4.1.4. Comparison of X-Band with C-Band with respect to detectability of V-narrow wakes

Similar to Kelvin wake arms the $\overline{DLM_{VW,RS2}} \approx \overline{DLM_{VW,S1}} \approx 0$ and its low $\overline{RMSE_{VW,S1}}$ and $\overline{RMSE_{VW,RS2}}$ imply that almost all wake samples did not show any signature of V–narrow wakes in S1 and R2 imagery. In contrast, the uncertainties $\overline{RMSE_{VW,S1}}$ and $\overline{RMSE_{VW,RS2}}$ are so low that the high uncertainties $\overline{RMSE_{VW,TSX}}$ and especially $\overline{RMSE_{VW,CSK}}$ are not relevant, as $\overline{RMSE_{VW,s_n}} < \overline{\Delta\widehat{DLM}_{VW,s_n,s_m}}, \forall s_n \in \{TSX, CSK\}, \forall s_m \in \{S1, RS2\}$ and $\overline{RMSE_{VW,s_m}} < \overline{\Delta\widehat{DLM}_{VW,s_m,s_n}}, \forall s_n \in \{TSX, CSK\}, \forall s_m \in \{S1, RS2\}$.

The qualitative uncertainty analysis in the Fig. 9 shows clearly separable histogram peaks of C–Band histograms from X–Band histograms. In conclusion, the difference in detectability of V–narrow wakes between C–Band and X–Band is found to be significant.

As a low level of uncertainty of the detectability models for V-narrow wakes is encountered, the results are significant and no alternative analysis is required. Anyway, the characteristic pattern of V–Narrow wakes with the small angle of ~ 2° between the V–narrow wake arms is not resolved in the superimpositions of backscatter intensities.

4.1.5. Summary of detectability comparison between X-Band and C-Band

As discussed in the previous Subsections 4.1.1, 4.1.2 and 4.1.3 near-hull turbulences, turbulent wakes and Kelvin wake arms were not found significantly better detectable in X–Band than in C–Band imagery. However, according to the Subsection 4.1.4, V–narrow wakes are significantly better detectable in X–Band than in C–Band imagery. Due to the high proportion of V–Narrow wake arms (see Table 1) in the X-Band datasets, it is therefore concluded that X–Band is better suited for the detection of ship wakes than C–Band.

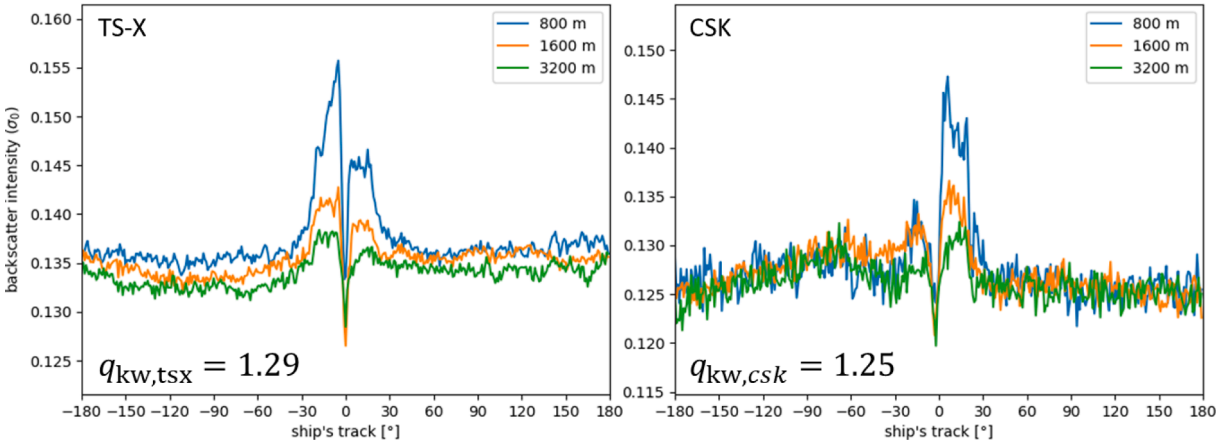

Fig. 12. Distribution of mean backscatter intensities of superimpositions based on low incidence angles in the range of 20° to 30° for Kelvin wake arms; no samples available for S1 and RS2 with this image acquisition setting; the curves for the 200 m and 400 m radial bins are not displayed. (For interpretation of the references to colour in this figure legend, the reader is referred to the web version of this article.)

4.2. Comparison of detectability between shorter and longer slant range missions

In this subsection the research question RQ2 is discussed, separately for each wake component in 4.2.1 to 4.2.4 and generally in 4.2.5.

4.2.1. Comparison of shorter and longer slant ranges with respect to detectability of near-hull turbulences

Fig. 5(a) shows that $\overline{DLM_{NT,S1}} > \overline{DLM_{NT,RS2}} > \overline{DLM_{BT,CSK}} > \overline{DLM_{NT,TSX}}$. So, only on the basis of mean DLM, the two sensors with longer slant ranges would perform even better on the detection of near-hull turbulences than the two sensors with shorter slant ranges. However, as already explained in Subsection 4.1.1, no significant differences between the sensors can be concluded after analysis of model's uncertainties and distribution of backscatter intensities in the superimpositions.

4.2.2. Comparison of shorter and longer slant ranges with respect to detectabilty of turbulent wakes

As already described in Subsection 4.1.2, CSK performs significantly better on the detection of turbulent wakes than S1 and RS2, but TSX with even shorter slant ranges than CSK and S1 with shorter slant range than RS2 does not. Therefore, no significant difference in detectability between sensors with shorter and longer slant ranges can be concluded.

4.2.3. Comparison of shorter and longer slant ranges with respect to detectabilty of Kelvin wake arms

In Subsection 4.1.3 was already stated that the difference in detectability is attributed to slant ranges instead of radar frequencies. Although the slant ranges differ between TSX, CSK and S1 in Fig. 13 the characteristic Kelvin wake pattern is similarly well recognizable. For RS2 with its significantly longer slant ranges the characteristic pattern cannot be recognized. Therefore, it is assumed that the decrease in detectability of Kelvin wake arms with increasing slant ranges is nonlinear. Rather the detectability drops significantly at longer slant ranges.

4.2.4. Comparison of shorter and longer slant ranges with respect to detectability of V-narrow wakes

V–narrow wakes are significantly better detectable in X-Band imagery than in C-Band imagery (see Subsection 4.1.4). But, in contrast to Kelvin wake arms no significant difference between RS2 and S1 can be recognized and the difference between TSX and CSK is even reversed. Therefore, the difference in detectability is attributed to the different radar frequencies, not to the different slant ranges.

4.2.5. Summary of detectability comparison between shorter and longer slant ranges

Only for Kelvin wake arms the difference in detectability can be attributed to the different slant range. For the other wake component based on Bragg scattering, the V-Narrow wake, also a lower detectability

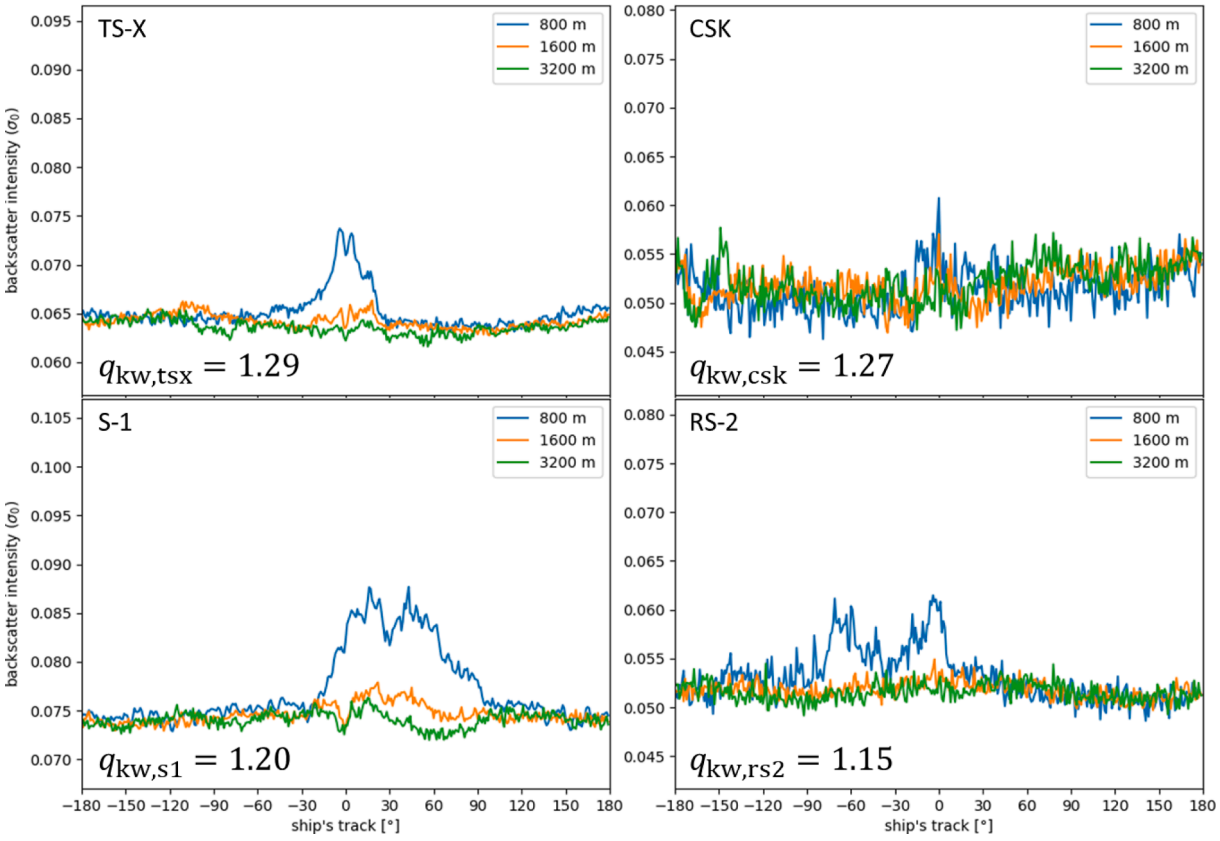

Fig. 13. Distribution of mean backscatter intensities of superimpositions based on low incidence angles in the range of 30° to 40° for Kelvin wake arms; the curves for the 200 m and 400 m radial bins are not displayed. (For interpretation of the references to colour in this figure legend, the reader is referred to the web version of this article.)

Table 5
Summary on detectability of four ship wake components by different SAR sensors.

Ship wake components	Summary on differences in detectability Not better suited= "-" Better suited = "+"	
	X-band better suited than C-band?	Shorter slant range better suited than longer slant range?
near-hull turbulence (4.1.1, 4.2.1)	–	–
turbulent wakes (4.1.2, 4.2.2)	–	–
Kelvin wake arms (4.1.3, 4.2.3)	–	+
V–narrow wake (4.1.4, 4.2.4)	+	–
In general (4.1.5, 4.2.5)	+	+

in imagery of sensors with longer slant ranges can be observed, but the difference is not significant. As Kelvin wake arms are observable in roughly-one third of TSX images and the majority of CSK images, it can be concluded that shorter slant ranges are generally better suited for the detection of ship wakes.

4.3. Summary

X-Band radar frequencies or shorter slant ranges are better suited for the detection of ship wakes than C–Band radar frequencies or longer slant ranges. However, this general conclusion is only based on the differences in detectability, which were encountered for Kelvin wake arms and V–narrow wakes. For those wake component the respective research questions lead to different conclusions. The conclusions of the previous subsections are summarized in Table 5.

5. Conclusions

In this study, the differences in detectability of wake components between four SAR sensors are evaluated. For that purpose, quantitative and qualitative analyses were conducted and a measure for the detectability models' uncertainties was introduced. The two research questions RQ1 and RQ2 can now be concluded.

The analyses of this study show that near-hull turbulences and turbulent wakes are neither significantly affected by C–Band or X–Band radar frequencies nor by shorter or longer slant ranges.

It was concluded that Kelvin wakes arms are significantly better detectable under shorter slant ranges. Kelvin wakes are the wake components, which consist of various systems of gravity waves. This means, varying surface slopes and orbital motions are present so that Kelvin wakes are connected to the scattering mechanisms of tilt modulation, hydrodynamic modulation and velocity bunching (Holt, 2004). Especially the velocity bunching effect is dependent on the slant range: With increasing slant range also the nonlinear distortions of velocity bunching become more prominent, because the azimuth shift of moving point targets becomes larger. With respect to ocean waves it is known that such distortions can completely destroy the imaged ocean wave pattern (Hennings et al., 1999; Holt, 2004). Analogically, the characteristic pattern of Kelvin wakes can be destroyed, resulting in decreased detectability. This relationship between Kelvin wakes and velocity bunching explains, why detectability of Kelvin wakes decreased with increasing slant ranges.

From the analyses of V–narrow wake arms were concluded that they are significantly better detectable by X–Band SAR sensors than by C-Band SAR sensors. All other wake components are connected to a variety of scattering mechanisms, i.e. Rayleigh and Bragg scattering, specular, dihedral and corner reflection as well as the already mentioned tilt modulation, hydrodynamic modulation and velocity bunching (Holt, 2004; Thompson, 2004). The development of V-Narrow wakes is only the result of Bragg Scattering. This explains, why the detectability of this wake component is found most dependent on the radar frequency band, in contrast to the other wake components. The radar frequency band determines the first and higher order Bragg wavelength, which must be met by the circularly propagating waves on the V-narrow wakes arm's regions (Lyden, et al., 1988; Reed & Milgram, 2002). In conclusion, the longer Bragg wavelengths of C–Band sensors are more difficult to meet than the shorter Bragg wavelengths of X–Band sensors.

However, it was also shown that also V–narrow wakes are better detectable under shorter slant ranges and that also Kelvin wake arms are better detectable by X-Band SAR sensors, but those differences were found to be insignificant during the uncertainty analysis. Both wake components are based on Bragg scattering. Due to this similarity and the fact that those differences are recognizable, even though not significant, it can generally be concluded that slant ranges and radar frequencies have an effect on both wake components. From the results, it is further concluded that the detectability of those two wake components does not linearly decrease with increasing slant ranges.

The generally better detectability of ship wakes in TSX imagery compared to RS2 and S1 imagery, which was stated in (Tings & Velotto, 2018), can now be explained: Both Bragg-based wake components have considerable proportions in the datasets. Therefore, the detectability of ship wakes increases generally, when sensors with shorter slant ranges and X-Band instead of C-Band radar frequencies are used.

The additionally introduced CSK dataset showed the best performance with respect to wake detection for turbulent wakes and Kelvin wake arms. However, as a high level of uncertainty was encountered during all analyses of this dataset, this peculiarity is discarded.

The presented analyses rely on a manual inspection procedure executed by humans. So, it cannot be ruled out that a human error is involved. The intention of uncertainty analysis and the provision of an alternate analysis of distribution of backscatter intensities is to mitigate this human error. Various methods for fully automatic wake detection exist, but those methods detect individual wake components, only when wake signatures are well developed (Graziano et al., 2016). Once robust methods for wake component detection are developed, the presented analysis could be repeated with less human error involved.

Declaration of Competing Interest

The authors declare that they have no known competing financial interests or personal relationships that could have appeared to influence the work reported in this paper.

Acknowledgements

A Special thanks goes to Dr. James Imber for serving as partner for fruitful discussions and providing his knowledge in the field of machine learning.

This research did not receive any specific grant from funding agencies in the public, commercial, or not-for-profit sectors.

Appendix

Table A1
List of abbreviations and variables.

Abbreviation	Meaning
TSX	TerraSAR–X
CSK	CosmoSkymed
RS2	RADARSAT–2
S1	Sentinel–1
CCDF	Complementary Cumulative Distribution Function
CDF	Cumulative Distribution Function
DLM	Detectable Length Metric
NT	Near-hull turbulence
TW	turbulent wake
KW	Kelvin wake arms
VW	V–narrow wakes
R	slant range
θ	incidence angle
h	orbit altitude
x_i	influencing parameters with index $i = 1,\ldots,5$
i	Index of influencing parameter
x_i	influencing parameters with index $i = 1,\ldots,5$
Δx_i	$x_i^{max} - x_i^{min}$
w	wake component nominator
W	set of wake component $\{\mathrm{NT}, \mathrm{TW}, \mathrm{KW}, \mathrm{VW}\}$
s	satellite nominator
S	Set of satellite {TSX,CSK,S1,RS2}
$l_{w,s}$	wake component length
l_w^{min}, l_w^{max}	wake component length boundaries for linear normalization of wake component length into DLM
$l'_{w,s}$	truncated $l_{w,s}$ ($l_{w,s}$ cropped to l_w^{min} and l_w^{max})
$DLM_{w,s}$	Detectable Length Metric for each wake component and satellite
V	volume defining multidimensional integration over the five-dimensional feature space
$\overline{DLM_{w,s}}$	Averaged Detectable Length Metric over feature space V
$f_{w,s}$	detectability SVR model (hyperplane) for each wake component and satellite
$D_{w,s}$	dataset with wake samples for each wake component and satellite
$D_{w,s}^j$	subsets of dataset $D_{w,s}$ split into n subsets denoted with index $j \in \{j \in \mathbb{N} \vert 1 \leq j \leq n\}$.
n	amount of data subsets for each dataset
$f_{w,s}^j$	detectability model trained for subset $D_{w,s}^j$.
$f_{w,s}^o$	each model $f_{w,s}^j$ is contrasted against the respective other four models with index $o \in \{o \in \mathbb{N} \vert 1 \leq o \leq n \bigwedge o \neq j\}$
j	subset index
o	other subset index
$\mathrm{RMSE}_{w,s}^{j,o}$	uncertainty expressed by root mean square error calculated for each pair of hyperplanes $\left(f_{w,s}^j, f_{w,s}^o\right)$
$\overline{RMSE_{w,s}}$	overall uncertainty averaged over all $\mathrm{RMSE}_{w,s}^{j,o}$
m	amount of pairs of hyperplanes for retrieval of $\overline{RMSE_{w,s}}$
$\overline{\Delta DLM_{w,s_1,s_2}}$	mean difference of detectability between two sensors s_1 and s_2
$\overline{\widehat{\Delta DLM_{w,s_1,s_2}}}$	averaged mean difference of detectability between multiple data subsets of two sensors s_1 and s_2
$S_{w,s,k}$	image with superimposition of pixel intensities for each wake component, sensor and data subset k
k	subset index for superpositions
$P_{\alpha,r}$	set of pixels around wake's origin point within angular bin α and radial bin r
α	angular bin
r	radial bin
$\overline{S_{w,s,i}}(\alpha, r)$	mean intensity over all pixels in angular bin α and radial bin r
$I_{clutter,s,i}$	set of intensity values of all pixels considered as clutter
$I_{w,s,i}$	set of intensity values of all pixels considered part of wake component
$\mu_{clutter,s,i}$	mean clutter intensities
$\mu_{w,s,i}$	mean wake component intensities
$q_{w,s,i}$	ratios of clutter's and wake component's mean intensity, $q_{w,s,i} = \mu_{w,s,i}/\mu_{clutter,s,i}$

References

Canadian Space Agency (CSA), 2019. *Canadian Space Agency*. [Online] Available at: https://asc-csa.gc.ca/eng/satellites/radarsat/technical-features/radarsat-comparison.asp[Accessed 20 July 2020].

Alpers, W.R., Ross, D.B., Rufenach, C.L., 1981. On the detectability of ocean surface waves by real and synthetic aperture radar. J. Geophys. Res. 86, 6481–6498.

Darmon, A., Benzaquen, M., Raphaël, E., 2014. Kelvin wake pattern at large Froude numbers. J. Fluid Mech. 738 (R3).

Dysthe, K.B., Trulsen, J., 1989. Internal Waves from Moving Point Sources. John Hopkins APL Technical Digest 10 (4), 307–317.

European Space Agency (ESA), 2020. *ESA Sentinel Online*. [Online] Available at: https://sentinels.copernicus.eu/web/sentinel/missions/sentinel-1[Accessed 20 July 2020].

Gade, M., et al., 1998a. Imaging of biogenic and anthropogenic ocean surface films by the multifrequency/multipolarization SIR-C/X-SAR. J. Geophys. Res. 103 (C9), 18851–18866.

Gade, M., et al., 1998b. On the Reduction of the Radar Backscatter by Oceanic Surface Films: Scatterometer Measurements and Their Theoretical Interpretation. Remote Sens. Environ. 66 (1), 52–70.

Graziano, M.D., 2020. Preliminary Results of Ship Detection Technique by Wake Pattern Recognition in SAR Images. Remote Sens. (Basel) 12 (18), 2869.

Graziano, M.D., D'Errico, M., Rufino, G., 2016. Wake Component Detection in X-Band SAR Images for Ship Heading and Velocity Estimation. Remote Sens. (Basel) 8 (6), 498.

Hennings, I., Romeiser, R., Alpers, W., Viola, A., 1999. Radar imaging of Kelvin arms of ship wakes. Int. J. Remote Sens. 20 (13), 2519–2543.
Hogan, G., Chapman, R., Watson, G., Thompson, D., 1996. Observations of Ship-Generated Internal Waves in SAR Images from Loch Linnhe, Scotland and Comparison with Theory and in situ Internal Wave Measurements. IEEE Trans. Geosci. Remote Sens. 34 (2), 532–542.
Italian Space Agency (ISA), 2007. *About COSMO-SkyMed.* [Online] Available at: http://www.cosmo-skymed.it/en/index.htm[Accessed 21 July 2020].
Holt, B., 2004. Chapter 2. SAR Imaging of the Ocean Surface. In: NOAA, Hrsg. *Synthetic Aperture Radar Marine User's Manual.* U.S. Department of Commerce, Washington, DC, pp. 25–79.
Lyden, J.D., Hammond, R.R., Lyzenga, D.R., Shuchman, R., 1988. Synthetic Aperture Radar Imaging of Surface Ship Wakes. J. Geophys. Res. 93 (C10), 12293–12303.
McCandless, S.W., Jackson, C.R., 2004. Chapter 1. Principles of Synthetic Aperture Radar. In: Synthetic Aperture Radar Marine User's Manual. U.S. Department of Commerce, Washington, DC, pp. 1–23.
Milgram, J.H., Peltzer, R.D., Griffin, O.M., 1993. Supression of Short Sea Waves in Ship Wakes: Measurements and Observations. J. Geophys. Res. 98 (C4), 7103–7144.
Oumansour, K., Wang, Y., Saillard, J., 1996. Multifrequency SAR observation of a ship wake. IEE Proceedings - Radar, Sonar and Navigation 143 (4), 275–280.
Pichel, W.G., Clemente-Colón, P., Wackerman, C.C., Friedman, K.S., 2004. Chapter 12. Ship and Wake Detection. In: Synthetic Aperture Radar Marine User's Manual. U.S. Department of Commerce, Washington, DC, pp. 277–303.
Pitz, W., Miller, D., 2010. The TerraSAR-X Satellite. IEEE Trans. Geosci. Remote Sens. 2, 615–622.
Pleskachevsky, A., Tings, B., Wiehle, S., Jacobsen, S., 2022. Multiparametric sea state fields from synthetic aperture radar for maritime situational awareness. Remote Sens. Environ. 280, 113200.
Rabaud, M., Moisy, F., 2013. Ship wakes: Kelvin or Mach angle? Phys. Rev. Lett. 110 (21).
Reed, A.M., Milgram, J.H., 2002. Ship Wakes and Their Radar Images. Annu. Rev. Fluid Mech. 34, 469–1402.
Soloviev, A., et al., 2010. Sonar Measurements in Ship Wakes Simultaneous With TerraSAR-X Overpasses. IEEE Trans. Geosci. Remote Sens. 48 (2), 841–851.
Thompson, D.R., 2004. Chapter 4. Microwave scattering from the sea. In: NOAA, Hrsg. *Synthetic Aperture Radar Marine User's Manual.* U.S. Department of Commerce, Washington, DC, pp. 117–138.
Tings, B., et al., 2020. X-Band/C-Band-Comparison of Ship Wake Detectability. MDPI, Leipzig.
Tings, B., 2021. Non-Linear Modeling of Detectability of Ship Wake Components in Dependency to Influencing Parameters Using Spaceborne X-Band SAR. Remote Sens. (Basel) 13 (2), 165.
Tings, B., 2022. Research Data for "Comparison of detectability of ship wake components between C-Band and X-Band synthetic aperture radar sensors operating under different slant ranges". Mendeley Data V2. https://data.mendeley.com/datasets/xxzmb73x27/2.
Tings, B., Bentes, C., Velotto, D., Voinov, S., 2018. Modelling Ship Detectability Depending On TerraSAR-X-derived Metocean Parameters. CEAS Space Journal.
Tings, B., Pleskachevsky, A., Velotto, D., Jacobsen, S., 2019. Extension of ship wake detectability model for non-linear influences of parameters using satellite based X-band synthetic aperture radar. Remote Sens. 11 (5), 563.
Tings, B., Velotto, D., 2018. Comparison of ship wake detectability on C-band and X-band SAR. Int. J. Remote Sens. 1–18.
Tunaley, J.K.E., Buller, E.H., Wu, K.H., Rey, M.T., 1991. The Simulation of the SAR Image of a Ship Wake. IEEE Trans. Geosci. Remote Sens. 29 (1), 149–156.
Wang, J.-K., Zhang, M., Cai, Z.-H., Chen, J.-L., 2017. SAR imaging simulation of ship-generated internal wave wake in stratified ocean. J. Electromagn. Waves Appl. 31 (11–12), 1101–1114.
Zilman, G., Miloh, T., 1997. Radar Backscatter of a V-like Ship Wake from a Sea Surface Covered by Surfactants. In: Washington, D.C. (Ed.), Twenty-First Symposium on Naval Hydrodynamics. The National Academies Press, pp. 235–248.